Fall 2019

Designing, Constructing, and Employing Two-Dimensional Ultrafast Spectroscopy to Resolve Complex Kinetics

Jason R. Darvin

DESIGNING, CONSTRUCTING, AND EMPLOYING TWO-DIMENSIONAL ULTRAFAST SPECTROSCOPY TO RESOLVE COMPLEX KINETICS

by

Jason R. Darvin

Bachelor of Science
Auburn University, 2013

Submitted in Partial Fulfillment of the Requirements

For the Degree of Doctor of Philosophy in

Chemistry

College of Arts and Sciences

University of South Carolina

2019

Accepted by:

Mark Berg, Major Professor

Andrew Greytak, Committee Member

S. Michael Angel, Committee Member

Yanwen Wu, Committee Member

Cheryl L. Addy, Vice Provost and Dean of the Graduate School

DEDICATION

This dissertation is dedicated to my wife, Bethany, my son, Caden, and my parents who supported me and encouraged me throughout graduate school.

ACKNOWLEDGEMENTS

My Ph.D. education would not have been possible without the help and guidance of several people.

I would first like to thank my advisor, Prof. Mark Berg. His guidance and mentorship was invaluable throughout my graduate career. He was always available to offer helpful hints and solutions to solve problems I faced during my research. He was also willing to listen to problems in my person life when I needed to talk. His support allowed me successfully complete my education.

I would like to thank my Ph.D. committee, Prof. Andrew Greytak, Prof. Mike Angel, and Prof. Yanwen Wu. Each of them was willing to speak with me and offer guidance during my graduate career.

I would also like to thank my colleagues, Dr. Haorui Wu, Dr. Sachin Verma, Harveen Kaur, Mainak Dhar, and Stuart Hodge. Working with all of you has been a pleasure. In addition, I want to thank the National Science Foundation for their economic support my research projects.

Finally, I would like to thank my family. My wife provided constant support during my collegiate education. I would like to thank my parents for their support. Without them, I would not have been able to complete my Ph.D.

ABSTRACT

Multiple population-period transient spectroscopy (MUPPETS) is a two dimensional ultrafast time resolved spectroscopy technique. MUPPETS uses three pairs of optical pulses over two time periods to separate homogeneous and heterogeneous causes of rate dispersion. This dissertation details improvements to the MUPPETS optical assembly enabling measurements on systems that previously fell outside of the MUPPETS 2-ns time window. In addition, the theoretical groundwork is laid to unveil the hidden coordinate controlling rate exchange using 2D and 3D correlation functions.

The first project details improvements made to the MUPPETS assembly. A detailed method was developed to eliminate astigmatism, coma, and spherical aberration from the MUPPETS optical assembly. A slow response photodiode was built to correct for long term power fluctuations in MUPPETS signals. A double modulation scheme was introduced by the addition of a second chopper to eliminate the detection of background signals. In addition, other concerns are discussed.

The second project develops a simple, but general, model that allows multidimensional correlation functions to be calculated for systems that exhibit nonexponential kinetics. Nonexponential kinetics imply the existence of at least one slow variable other than the observable, that is, the system has a "hidden" coordinate. Homogeneous and heterogeneous mechanisms are both included, and slow exchange of the rates is allowed. This model shows that 2D and 3D correlation functions of the observable measure the distribution and kinetics of the hidden coordinate controlling rate

exchange. Both the mean exchange time and the shape of the exchange relaxation are measurable.

The fourth project utilizes the rotation of PM597 to probe the local properties of SDS micelles. In traditional 1D experiments, solute rotation in micelles is known to exhibit rate dispersion. This rate dispersion has commonly been attributed to local anisotropy or heterogeneity in the local viscosity. Polarized MUPPETS is used to resolve this conflict. This 2D technique shows that heterogeneity in the local viscosity is responsible for 87% of the rate dispersion in opposition of the more widely accepted "wobble-in-a-cone" model. This result suggests that on the subnanosecond timescale, the solute sees only one strong fluctuation of the micelle structure.

The final project measures the rotation anisotropy of PM597 with polarized pump-probe spectroscopy in a variety of ionic liquids and concentrations. The rotation of PM597 is measured in C_nMIM:BF_4 ($\chi = 0.2$) and acetonitrile, where n = 2, 4, 8, and 12. In addition the rotation of PM597 was measured in acetonitrile and C_{12}MIM:BF_4 at $\chi = 0.0$, 0.2, 0.4, and 0.6. Rate dispersion was measured in sample; however, the magnitude of rate dispersion was within the noise level of the MUPPETS experiment.

TABLE OF CONTENTS

LIST OF TABLES

LIST OF FIGURES

LIST OF ABBREVIATIONS

C ..... chopper

C_2MIM:BF_4 ..... 1-ethyl-3-methylimidazolium tetrafluoroborate

C_4MIM:BF_4 ..... 1-butyl-3-methylimidazolium tetrafluoroborate

C_8MIM:BF_4 ..... 1-octyl-3-methylimidazolium tetrafluoroborate

C_{12}MIM:BF_4 ..... 1-dodecyl-3-methylimidazolium tetrafluoroborate

G ..... grating

L ..... lens

ML ..... meniscus lens

MUPPETS ..... Multiple Population-Period Transient Spectroscopy

ND ..... neutral density

PD ..... photodiode

P ..... polarizer

PM597 ..... pyrromethene 597

PP ..... phase plates

SDS ..... sodium dodecyl sulfate

VND ..... variable neutral density

WP ..... waveplates

CHAPTER 1

INTRODUCTION

1.1 Overview

Non-exponential kinetics often arise as chemical processes become more complex. When a chemical process possesses a non-exponential rate decay, the presence of multiple rates is implied. Such a process is known to exhibit rate dispersion. Two general mechanisms are capable of resolving the cause(s) of rate dispersion. In the first mechanism, the decay of individual molecules is inherently non-exponential where every molecule undergoes a multistep relaxation process. This model is homogeneous. In the second mechanism, sub-ensembles of the system experience an exponential relaxation process. Averaging of different sub-ensembles results in an overall non-exponential decay. This model is heterogeneous. Standard one-dimensional experiments are capable of measuring the magnitude of rate dispersion present; however, they are not capable of resolving whether the underlying chemical process is homogenous or heterogeneous in nature.

The Berg group employs a two-dimensional ultrafast spectroscopy technique known as MUPPETS (Multiple Population-Period Transient Spectroscopy) which is capable of separating homogeneous and heterogeneous causes of rate dispersion. This dissertation discusses four topics: 1) Technical improvements made to the MUPPETS experiment to allow for measurements on more complicated systems. 2) The generation of a model that allows multidimensional correlation functions to measure the exchange time

of subensemble populations in systems that exhibit heterogeneous rate dispersion. 3) The discovery of rate heterogeneity in sodium dodecyl sulfate (SDS) micelles by measuring the rotational anisotropy of a solute molecule. 4) The anisotropy of solute rotation in ionic liquids.

The work described within produced two published articles and relate to Chapters 3 and 4. Chapter 2 discusses the technical improvements that were required to study more complex systems with MUPPETS and the techniques used to eliminate optical aberrations from the optical setup. Chapter 3 discusses the generation of a model used to extract information from multidimensional correlation functions and is published as: Berg, M. A.; Darvin, J. R. *Journal of Chemical Physics* **2016**, *145*, 054119. Chapter 4 discusses the measurement of rate heterogeneity in SDS micelles and is published as Darvin, J. R.; Berg, M. A. *J. Phys. Chem. Lett.* **2019**, *10*, 6885-6891. Chapter 5 discusses the anisotropy of solute rotation in ionic liquids. An additional journal article is anticipated that includes the results from Chapter 4 and results from experiments in progress on a second micelle system.

1.2 Multiple Population-Period Transient Spectroscopy

Multiple Population-Period Transient Spectroscopy (MUPPETS) is a two-dimensional time resolved spectroscopy technique that is capable of resolving the cause of rate dispersion on the picosecond time scale across the evolution of two time periods. A schematic for the MUPPETS experiment is shown in Figure 1.1a and is described as follows: Two simultaneous laser pulses (1*b* and 1*c*) enter the sample at an angle intersecting to form a spatial grating of excited states (red). After a time τ_2, a second pair of simultaneous pulses (2*a* and 2*b*) create a second spatial grating (blue) in the opposite

direction. Molecules that interacted with each pulse pair (black) form a vertical grating. After a second time τ_2, pulse 3*c* is diffracted from the vertical plane formed by the black regions. The diffracted signal is combined with pulse 3*a* for heterodyne detection. Diffraction from the black regions permits only the signal caused by the interaction of pulse pair 1 and pulse pair 2 to be measured. In the MUPPETS experiment, the first time period, τ_1, is set a fixed time delay. The signal is then measured by varying the second time period τ_2. As the fixed time τ_1 is increased, fast decaying molecules present in the system will decay to the ground state while slowly decaying molecules remain in the excited state; therefore, increasing the fixed time τ_1 allows slower sub-ensembles to be isolated and measured. In other words, τ_1 acts as a rate filter enabling the detection of rate heterogeneity.

The experiment described above requires six laser pulses. In theory, the same measurements could be made with only three laser pulses; however, the six pulse geometry (Figure 1.1b) allows lower order two, three, and four beam signals to be removed due to mismatched wave-vectors. The optical assembly required for the MUPPTES experiment is shown in figure 1.2. Polarization control of each pulse pair allows the rotational dynamics of probe molecules to be measured.

1.3 Measuring a Hidden Coordinate: Rate Exchange Kinetics from 3D Correlation Functions

Rate dispersion has been observed in a variety of systems such as supercooled liquids, polymers, biomolecules, ionic liquids, microstructures, and nanoparticles. The presence of rate dispersion indicates a non-Markovian system. In a Markovian process, the future states of the system are independent of the past states of the system; thus, a non-

Markovian process implies a "hidden coordinate" that retains memory of the past is present. The goal is to determine the physical process responsible for the hidden coordinate; however, it cannot be directly observed.

One-dimensional experiments measure a systems evolution over one time interval. They are capable of measuring the mean rate and quantifying the total rate dispersion. They cannot assign the rate dispersion to specific processes. Two-dimensional measurements measure a systems evolution over two time intervals and are capable of determining the fraction of rate dispersion that is due to heterogeneity. The rates of the different sub-ensembles can be used to determine the probability distribution of the hidden coordinate. In systems that equilibrate, a single molecule will eventually experience all of the rate sub-ensembles. This known as rate exchange. No known experiments are able to measure rate exchange.

Three-dimensional correlations functions have been used in the past to quantify rate exchange; however, the methods are not rigorous and could yield incorrect results. This project developed a model that is general enough to apply to real systems and simple enough to calculate multidimensional correlation functions. The model contains heterogeneous and homogeneous contributions to rate dispersion. It also includes exchange between different sub-ensembles that is slow relative to the decay of the observable. This model allows well defined measures of the rate exchange dynamics to be made and is able to separate that information from contributions cause by other rate altering pathways.

1.4 Micelle Heterogeneity from the 2D Kinetics of Solute Rotation

In microstructured materials, the photophysics of solute molecules are used to infer local properties. The rotation time of a solute can be used to characterize the local viscosity

in micelles by measuring the optical anisotropy. However, in micelles, the one-dimensional anisotropy is non-exponential meaning that rate dispersion is present. A simple explanation for the rate dispersion is that is reflects rate heterogeneity. Solute molecules could occupy different positions within a micelle and experience a different local viscosity. In this scenario, each solute would have a defined rotation time and experience a specific micoviscosity. A contrasting, but widely accepted, explanation is the "wobble-in-a-cone" model. This model is homogeneous, and it assumes that every micelle has the average structure, which is strongly layered into a hydrocarbon core, a surface layer of partially hydrated head groups, and the aqueous solvent. It further assumes that the probe is confined to the surface layer, and this layer is strongly anisotropic. Each solute can only "wobble" over a restricted cone of angles at fast times. Large angles are explored by diffusion around the micelles at long times. In this model, each solute experiences the fast and slow process. One-dimensional experiments cannot distinguish between the competing models.

Polarized MUPPETS is two-dimensional ultrafast spectroscopy that can separate homogeneous and heterogeneous processes. When using polarized pulses, there are four unique correlation functions differing by the type of dynamics measured in each time interval: rotation–rotation, electronic–electronic, symmetric rotation–electronic, and asymmetric rotation–electronic. The first two can be isolated with measurements at only two polarization combinations: $\Delta A_{++}(\tau_2, \tau_1)$ and $\Delta A_{-+}(\tau_2, \tau_1)$. In this study, pyrromethene 597 (PM597) was used as the solute inside sodium dodecyl sulfate (SDS) micelles. MUPPETS measurements were made to this system at nine τ_1 values. The resulting rotation–rotation surface shows that the 2D anisotropy rate increases systematically as τ_1 increases. This result indicates rate heterogeneity is important in the rotational dynamics.

A quantitative interpretation was performed using non-parametric statistical methods. These methods relied on a model generated from the measured 1D anisotropy and generated 2D decay spectra. Analysis of the decay spectra determined the fraction of the excess rate dispersion that is due to rate heterogeneity = 0.87. Further analysis created a possible distribution of microviscosities seen by the solute. The distribution suggests that a majority of the solutes experience a high local viscosity, much higher than the viscosity of dodecane, which is identical to the micelle tail. Because the center of the micelle, where viscosity would be the highest, occupies a small volume, it is unlikely the majority of solutes reside in the center of the micelle. Instead, the exclusion of water from the micelle interior constrains the motion of the SDS tails creating a high local viscosity. Micelles are held together by weak forces, which allows for large fluctuations in their instantaneous structures. Rate heterogeneity also arises from the diversity of structures from micelle to micelle.

1.5 Rotational Anisotropy in Ionic Liquids

Chapter 5 of this dissertation discusses a project that did not result in a publication. Ionic liquids (ILs) are organics salts that can exist in the liquid state. Because salts do not evaporate, ionic liquids have been considered for many industrial uses; however, ionic liquids exhibit non-exponential kinetics. Their dynamics are not well known. Solvation dynamics studies in micelles have shown the non-exponential kinetics are due to spatial heterogeneity caused by polar and non-polar regions within the liquid. Simulations back up this claim. Measuring the amount of heterogeneity in the rotation of a solute is a logical next step.

The 1D rotational anisotropy of PM597 was measured in several ILs. Because the rotation time of PM597 lies outside of our time resolution, acetonitrile was added to reduce the rotation time. In the first set of experiments, the mole fraction of ILs (χ = 0.2) was held constant and the chain length of the substituents on the imidazolium ILs (C_nMIM:BF_4) were varied (n = 2,4,8, and 12). In the second set of experiments, the mole fraction of the ionic liquid was varied. Rotation times became longer as the concentration of ionic liquid increased. All samples exhibited rate dispersion. Each IL exhibited similar non-exponential behavior. Ultimately, MUPPETS experiments were not performed on ILs because the amount of rate dispersion was less than expected. Increases in rotation times at long τ_1 values were expected to lie within the expected noise levels.

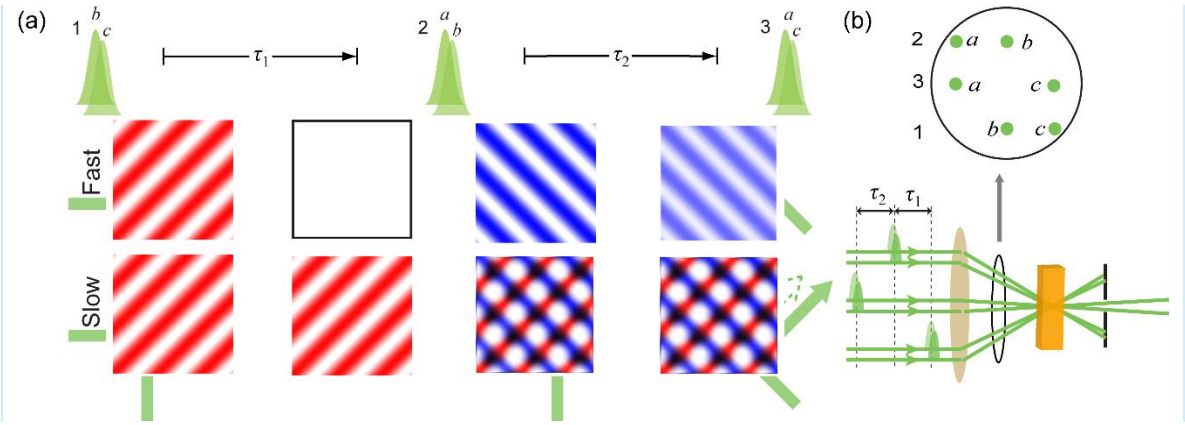

Figure 1.1 Schematic of the MUPPETS experiment. (a) The upper and lower panels represent fast and slowly relaxing subensembles within the sample. Two simultaneous pulses (1*b* and 1*c*) from different directions intersect in the sample to create a spatial grating of excited state molecules (red). After a time τ_1, a second pair of pulses (2*a* and 2*b*) create a second grating of excited molecules (blue). The slow subensemble now contains vertical diffraction planes formed by regions that interacted twice (black), once (red and blue), and never (white). After an additional time τ_2, pulse 3*c* is diffracted from these planes and is combined with pulse 3*a* for heterodyned detection. The diffraction isolates the signal unique to one interaction with the first excitation and one interation with the second excitation. (b) A representation for the pulse geometries used in the experiment. The brown circle is a lens. The orange cuboid represents the sample. The black circle shows a cross section with pulse lables.(Reproduced from Haorui Wu and Mark. A. Berg *J. Chem. Phys.* **2013**, *138*, 034201 https://doi.org/10.1063/1.4773982 with the permission of AIP Publishing.)

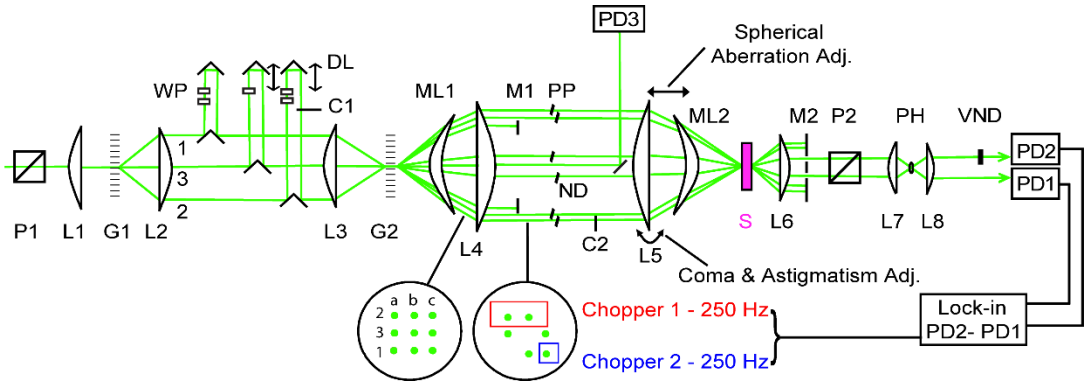

Figure 1.2 MUPPETS optical system: polarizers (P), lenses (L), gratings (G), delay lines (DL), meniscus lenses (ML), phase plates (PP), neutral density filter (ND), variable neutral density filter (VND), masks (M), sample (S), pinhole (PH), and photodiodes (PD). The locations of the coma and spherical aberrations adjustments are shown. The pulses chopped in the double modulation scheme are shown.

CHAPTER 2

MULTIPLE POPULATION-PERIOD TRANSIENT SPECTROSCOPY: THEORY AND TECHNICAL IMPROVEMENTS

2.1 Introduction

Multiple population-period transient spectroscopy (MUPPETS) is a multidimensional spectroscopy technique that utilizes a series of six laser pulses to isolate signals from desired sub-ensemble populations over two periods of time evolution. This technique enables the separation of homogeneous and heterogeneous processes in systems that exhibit non-exponential relaxation (rate dispersion). The current version of MUPPETS uses polarized optical pulses to measure the rotational anisotropy of solute molecules. The local viscosity of the surrounding medium governs the rotation rate of a solute molecule. By measuring the 2D anisotropy of a solute, polarized MUPPETS provides insight into the structure of materials or liquids on the nanometer scale.

Acquiring a MUPPETS signal requires a complex optical assembly that re-images the lines of a diffraction grating in the sample. Interferometric control of these spatial gratings is required to measure the MUPPETS signal. The concept of the assembly is shown in Figure 1.2. The optical assembly generates nine lasers pulses that share a single optical train. The use of a single optical train provides the necessary phase stability to perform the MUPPETS experiment; however, each optical component must be placed perfectly along

the optical axis to achieve spatial overlap of each laser pulse at the sample position. Slight deviations from the perfect position and alignment of each optical component leads to optical aberrations. Optical aberrations are a property of an optical system that cause deviations in the path of light in relation to the optical axis. Aberrations result in blurred images formed by the optical system. This chapter discusses three optical aberrations and the methods developed to eliminate them from the MUPPETS optical assembly. Astigmatism, chromatic, coma, and spherical aberration will be discussed. Laser beams are referenced in accordance with the naming scheme shown in Figure 1.2. In addition, several other improvements to MUPPETS are discussed. The work described here is fairly detailed and vital for one who must build a large, complex optical assembly; however, it is not appropriate for publication.

2.2 Optical Aberration Theory

This section discusses the theory of astigmatism, coma, and spherical aberrations.

2.2.1 Spherical Aberration

Spherical aberrations are found in optics with a spherical surface. In an optic with a spherical surface, the thickness and curvature of the lens varies with position. Light that interacts with the spherical surface off center will refract at different angle than light that interacts with the center. This results in different foci for light that interacts off center of the spherical surface. Spherical aberration can be reduced and/or eliminated by two methods. The first method uses at least one additional lens, such as a meniscus lens, to counteract the aberrations caused by a single spherical lens. The second lens is added to counteract the variation in angles on the spherical lens. The second method is to use an

aspheric lens. An aspheric lens has a surface profiles that are not spherical. In each case, the shape of the lens is designed by ray tracing software.

2.2.2 Comatic Aberration

Comatic aberrations, often referred to as coma, are cause by a lens that is off-axis (tilted) from the path of light. Coma causes light that interacts off-center of a tilted lens to focus at a different point and have a variation in magnification than light that interacts with the center of tilted lens. In a free space optical setup, such as a laser table, coma can be corrected by adding a tilt adjustment for angle of the lens.

2.2.3 Astigmatism

Astigmatism is an aberration that causes light propagating on orthogonal planes to have different focal lengths. It is similar to coma in that is can be caused by off axis beam propagation (tilted lenses). Astigmatism can be intentionally introduced to an optical system by the use of a cylindrical lens.

2.3 Diagnostic Design

This section discusses the diagnostic system used to eliminate optical aberrations in the MUPPETS optical assembly. This section and sections 2.4 and 2.5 discuss axes in the optical plane. The x-axis is defined as parallel to the laser table, the y-axis as perpendicular to the laser table, and the z-axis as the optical path.

2.3.1 Outside Laser Source

The process of eliminating optical aberrations from an optical system is easiest to achieve with a Gaussian laser pulse. Femtosecond laser systems require daily attention and great care to ensure the pulses remain Gaussian in shape. During the installation of an optical assembly, optical aberrations and/or misalignment can lead to blurred or distorted

images of a laser pulse when imaged onto a camera. This can lead to uncertainty in the beam profile of the ultrafast pulse. For that reason, it is beneficial to use a secondary laser source with a more reliable beam profile. Most commonly, gas lasers are utilized in the alignment of an optical system. However, our optical assembly is designed for 520-530 nm laser pulses. A typical HeNe laser would cause chromatic aberration in the MUPPETS optical assembly. Chromatic aberrations are caused by the diffraction of different wavelengths through refractive medium at slightly different angles. In the MUPPETS optical system, chromatic aberrations would also be introduced at G1 and G2 due to Bragg diffraction. Gas lasers that emit near 530 nm are expensive. For that reason, a 532 nm diode laser module was selected for the installation and alignment of the MUPPETS optical system.

2.3.2 Microscope Imaging System

The spatial gratings formed in the MUPPETS experiment are generated by reimaging the lines of G1 (Figure 1.1). The line width of the gratings used in the MUPPETS optical assembly is approximately 10 μm. To achieve a large enough signal size, 20 spatial gratings need to be generated in the sample; therefore, the spot size on G1 is required to be 200 μm. Imaging the laser beams at G2 and the sample requires the use of a microscope imaging systems to view the laser beams on a camera as they approach their focal point. A simple microscope setup was employed to view the beams on a CMOS camera. An aspheric lens must be used in the microscope to eliminate the possibility of optical aberrations in the imaging system. The lens is mounted with an opto-mechanical lens mount that has tilt corrections in the x-axis and y-axis of the optical plane. The lens mount is placed onto an opto-mechanical mount that has translation stages along the x-axis and z-axis of the optical

plane. The x-axis translation is used for alignment of the aspheric lens. The z-axis mount is used to adjust the focal point of the microscope. This method is preferable to moving the camera along the z-axis. A schematic of the microscope is shown in Figure 2.1. A magnifying power of 10 was used.

The positions along the optical path required to be imaged are important. Imaging two locations near each focal point is required to observe aberrations that are present in the optical system. The first, and most obvious, location to image is the focal point of the laser pulse(s) as determined by perfect lenses. The second location to image along the focal plane is just before the focal point where the laser pulses are separated and do not overlap. Identical mirror images should be formed at equal distances before and after the focal point. When the magnitude of the aberrations is large, they will be present when the laser beams are not overlapped. When the magnitude of the aberrations is small, viewing various combinations of laser pulses at the focal point is required to determine which aberrations are present. The positions in the optical assembly to be imaged will be discussed further in section 2.5.

Alignment of the diagnostic microscope is crucial. Misalignment of the aspheric lens will introduce aberrations to the diagnostic. Perfect alignment is achieved with the aid of a transmissive diffraction grating. The mount that houses the grating allows for rotation around the x-y plane. Transmissive diffraction gratings diffract light symmetrically in opposite directions. If the beams are not symmetric when viewed on the camera, then the aspheric lens is tilted. The diffraction from the grating must be viewed along the x-axis and y-axis to ensure the aspheric lens is not tilted in either direction. This method is more accurate than aligning the lens tilt via back reflections.

2.4 Intentional Examples of Optical Aberrations

Determining the types of optical aberrations present in an optical assembly can be difficult. Often times, after the initial installation of an optical system, multiple aberration will present themselves. The presence of more than type of aberrations can lead to uncertainty into what type of aberrations are present and which type dominates. Section 2.4 details what astigmatism, coma, and spherical aberrations look like in the MUPPETS optical assembly.

2.4.1 Astigmatism in MUPPETS

In the MUPPETS optical assembly, astigmatism can be generated by two methods. The first is in the installation of G1 and G2. The lines on G1 must be incident with the incoming laser beam. The lines on G2 must be opposite of incidence. Diffraction occurs on the surface with lines in a transmissive grating. This implies that the ±1 orders of diffraction travel through the diffractive optical material of G1. G2 must be installed so that the ±1 orders of diffraction generated by G1 travel through the optical material of G2 before diffraction occurs for a second time. Failure to install the transmissive gratings in this order will cause an astigmatism resulting in different foci for the sagittal and tangential planes along the optical axis.

The second manner in which an astigmatism can be generated is by improper positioning of L3 relative to G2. The three incoming laser beams onto G2 must overlap on the grating surface. When L3 is improperly positioned, the laser pulses will not overlap on G2. The focal point of the sagittal plane is defined as diffraction generated by G2. The focal point of the tangential plane is defined as the alignment of L3 relative to G2. G2 must

be positioned at the focal length of L3. An astigmatism can caused by translating L3 1 mm about the z-axis. An example is shown in Figure 2.2.

2.4.2 Comatic Aberration in MUPPETS

Comatic aberrations in the MUPPETS optical assembly are caused the by lens tilt relative to the optical axis. Coma may be caused by any of the lenses in the optical system, but lenses that contain more laser beams result in a greater amount of coma. Lenses in the optical assembly are mounted by epoxying each lens to an aluminum mount and then attached to magnetic opto-mechanical mounts for fixture to the laser table. Tilt in the x-axis could be caused by misalignment of the opto-mechanical mounts. Tilt in the x-axis or y-axis could be caused by unequal amounts of epoxy used to mount the lenses. Comatic aberrations in any combination of lenses in the MUPPETS optical assembly can eliminated by adding adjustable tilt to a single lens. Adding a mount that allows for adjustable tilt in the x-axis and y-axis to L5 counteracts coma caused by any other lens in the optical assembly. Figure 2.3 shows an example of coma by intentionally tilting L5 about the y-axis. Figure 2.3a shows coma when viewed 4 mm before the focal point as defined by perfect lenses. Lines have been added to emphasize the coma. Figure 2.3b shows the coma viewed at the focal point of beams 2a and 2c. It is clear that beams 1a and 1c possess a different focal point.

2.4.3 Spherical aberration in MUPPETS

Spherical aberrations in the MUPPETS optical assembly is caused by lens L4 and L5. Spherical aberration is corrected by the addition of two meniscus lenses, ML1 and ML2. Each meniscus lens must be shaped and positioned so that the spherical aberration caused by varying refractions angles on L4 and L5 is counteracted. An example of spherical

aberration in the MUPPETS optical assembly is shown in figure 2.4. ML2 was translated −1 cm along the z-axis of the optical plane. The image was taken 4 mm before the focal point. The added lines emphasize the spherical aberration.

2.5 Installation Method for the MUPPETS Optical Assembly

This section discusses, in detail, the methods required to eliminate optical aberrations from the MUPPETS optical assembly.

2.5.1 Defining the Optical Plane

The optical plane of an optical system must be defined before an optical assembly can be installed. The optical plane is defined by placing an iris before L1 and after P2. The holes on the optical table can be used to define the path parallel to side of the optical table. Two mirrors are used to align the femtosecond laser onto both irises simultaneously. Additional irises are placed before the predetermined locations of L3 and L5 to aid the installation of lenses. After the optical plane is defined, the outside laser source is inserted. It is inserted into the defined optical plane by using two additional mirrors to align it onto the irises before L1 and after P2.

2.5.2 Installation of the Optics before G2

The first lens (L1) is mounted with an opto-mechanical mount that has translation stage along the z-axis. The installation of L1 into the optical plane requires the alignment of the forward propagating laser beam and the backwards reflection from L1. The forward propagation should pass through two of the irises. The backward reflection should pass through the iris before L1. The initial position of G1 should be near the focal point of L1. The mount used with G1 has x-axis and y-axis tilt, translation on the x,y, and z planes, and rotation around x-y plane. The back reflections from G1 should be adjusted to go straight

back along the optical plane. At this point, the diagnostic setup is employed. The diffraction of G1 should be aligned along the y-axis of the optical plane. The spot size on G1 should completely fill the 200 μm pinhole that is on the surface of G1. Its position along the z-axis can be adjusted with the translatable mount on G1. The spot size can be confirmed by counting the number of grating formed by imaging the ±1 orders of diffraction at their focal point. Twenty gratings should be formed.

The installation of L2 is important. The three beams formed at G1 must propagate parallel to each other in between L2 and L3. The opto-mechanical mount for L2 contains a translation stage in the z-axis. When L2 is at its focal distance away from G1, the three laser beams will propagate parallel to each other. Measuring the correct distance exactly is difficult. To determine the correct location of L2, a mirror(s) can be used to view the laser beams a long distance. When L2 is in the correct position, it will be clear that the beams are parallel to each other. Once the beams are parallel, L3 can be installed.

2.5.3 Installation of G2 through ML2

The alignment of G2 should be performed with only one input beam. The back reflections are aligned with the tilt adjustment of the grating mount. The diffraction of G2 should be aligned along the x-axis of the optical plane. The alignment of the three laser beams onto G2 can be adjusted by the translation of L3. The nine laser beams generated at G2 should form a square pattern when viewed before the focal point. This is a good first approximation for the position on L3. The fine adjustment in the position is made by viewing select combinations of laser beams through a pinhole on the surface of G2. Laser beams 1b and 2b and beams 3a and 3c should have identical focal points when L3 is properly positioned. To determine if each pair of laser beams have an identical focal length,

cross sections of images for each pair can be plotted. Since beams 3a and 3c are formed by diffraction at G2, they should be used as the reference for beams 1b and 2b. When L3 is at the correct position, perfect gratings should be formed by both pairs of beams. When L3 is in an incorrect position, the gratings will be imperfect. This means the dark spots will not be completely dark as shown in Figure 2.5a When L3 is in the correct position, the dark spots will be completely dark as shown in Figure 2.5b. Cross sections of images can be obtained in MATLAB.

The installation of ML1, L4, L5, and ML2 is difficult and easiest achieved by a multistep process. The first critical step is to position ML1 and L4 so that the laser beams propagating from L4 are parallel. Once ML1 and L4 are installed, L4 should be translated along the z-axis until the beams propagate parallel to each other. Two 3.5" mirrors can be used to kick the beams across the room to check for parallel propagation. It is also crucial to ensure the laser beams do not clip the edge of the lens mounts. If the beams do clip the edge of the lens mounts, move ML1 and L4 closer to G2 along the z-axis and repeat the process over. It is important to note that the beams will expand when the delay lines are inserted. It is imperative to account for this when checking to see if any clipping occurs.

The diameter of the laser beams after G2 can be as large as 1.5 cm; thus, centering the beams on the lenses after G2 is quite difficult with L3 in place. The installation of ML1, L4, L5, and ML2 is easiest achieved by removing L3 and installing the lenses in the opposite order since beam 3 is collimated when L3 is not in place. Installing the optics in the reverse order allows back reflections to be aligned with greater accuracy. Great care must be taken to correctly replace L3. Employing the diagnostic a second time at G2 can give confidence L3 is accurately replaced.

The elimination of spherical aberration from ML1 and L4 is achieved by placing a 3.5" mirror after L4 and directing the laser beams straight back along the optical plane. The beams are steered into the microscope diagnostic with a pellicle beam splitter that has a thickness of 1 μm. The thinness of a pellicle beam splitter displaces the lasers beams a negligible amount. The nine laser pulses should be in a square pattern when spherical aberration is not present. When spherical aberration is present, the edge beams (beams 1b, 2b, 3a, and 3c) will have a different focal point than the corner beams (beams 1a, 1c, 2a, and 2c). The focal point, as determine by perfect lenses, should be determine by beams 3a and 3c since they are both generated on the surface of G2. If the magnitude of spherical aberration is large, a square pattern will not be seen when viewed before the focal point and will have a pattern similar to the example in Figure 2.4. Spherical aberration corrections are performed by translating ML1 along the z-axis. It is possible the z-axis micrometer on ML1 will not be able to translate a great enough distance. When this occurs, the opto-mechanical mount of ML1 must be moved by hand in the appropriate direction along the z-axis; however, it is likely ML1 will be aligned incorrectly. ML1, L4, L5, and ML2 will have to be reinstalled. The location of L4 should not change. The laser beams should still propagate parallel to each other in between L4 and L5. If a significant amount of coma is observed in ML1 and L2, the opto-mechanical mounts can be rotated around the x-z optical plane. Rotating optical mounts will likely result in the need to reinstall the optics. At this stage, if only a small amount of coma is present, it can be ignored. Coma will be eliminated later in the installation process.

After the elimination of spherical aberration from ML1 and L4, aberrations must be eliminated from L5 and ML2. The microscope diagnostic system must be setup at the

focal point of the optical system as defined by beams 3a and 3c (sample position). Spherical aberration is eliminated as described in the preceding paragraph. To eliminate coma, a pitch and yaw platform was added to the opto-mechanical mount of L5. Pitch refers to rotation about the y-axis, and yaw refers to rotation around the x-axis. The platform allows for ±4° around both the x-axis and y-axis. A combination of tilt about the x-axis and the y-axis is possible. Coma will be seen before the focal point if its magnitude is large. An example is shown in Figure 2.3. It is best to adjust the tilt of L5 one axes at a time if it appears coma is present in both the x and y planes. When an adjustment to the tilt is made, the lens must be translated along the same axes to keep the lens centered in the optical plane. Placing a reference point on the computer screen for beam 3b will aid translation adjustments. The process is continued until coma is eliminated.

Elimination of aberrations when the beams are viewed before the focal point is not sufficient. Various combinations of beams must be viewed at the focal point of beams 3a and 3c. The procedures detailed above will be followed to eliminate aberrations that are small in magnitude. The gratings formed by a combination of two beams can be evaluated by viewing cross sections of saved images. Combinations of three or more beams should be evaluated for consistency. The pattern should be consistent through the entire overlap of beams. Any inconsistency is caused by remaining aberrations. Detailed examination of two beam pairs will be required to determine the cause. A pinhole can be setup at the sample position with micrometers along the x, y, and z axes to map the path of individual beams. The center of an individual beam can be found by monitoring the intensity on a photodiode at various points along the z-axis. The x, y, and z reading of each micrometer must be recorded. Three dimensional scatter plots will yield great detail about the overlap

of the laser pulses at the sample position. Spherical aberration or coma adjustments can be made to improve the beam overlap.

2.6 Other Improvements to MUPPETS

Developing a method to eliminate optical aberrations from the MUPPETS optical assembly was not sufficient to perform the experiments discussed in Chapter 4. The complete anisotropy decay was not accessible to the two-nanosecond time window of the MUPPETS experiment. The signal size and stability of a six pulse experiment can depend on a variety of factors. These factors includes: long term fluctuations in the laser power, background signals that vary with power, minuscule variations in the laser alignment, or inaccurate alignment of the delay lines. Solutions to these problems are discussed in this section.

2.6.1 Slow Photodiode to Correct for Power Fluctuations

Femtosecond laser systems, especially those with nonlinear optical components, often experience power drift during the course of day. The MUPPETS experiment requires a sequence of eight measurements that lasts a duration of 4-5 hours. Power drift is expected to occur within that timeframe. To account for power drift in measured signals, a slow response photodiode was designed and constructed to measure and record the fluctuations in the laser power during experiments. The specifications of the photodiode's circuitry were designed to match the requirements of the lock-in detection system used to detect MUPPETS signals. The lock-in amplifier had two electronic requirements. The first was a 300 ms time constant. The second requirement was the electronic signal must have voltage in the range of ± 1 - 10 V. Silicon photodiodes typically have a response times in the nanosecond to microsecond range. Connecting the photodiode to a simple RC circuit can

increase the response time. The response time is characterized by $\tau = RC$, where τ is the response time (seconds), R is the resistance (Ohms), and C is the capacitance (Farad). This alone is not an adequate. The response is not always linear, and the voltage may not be great enough. An amplifier circuit solves both of these problems by guaranteeing a linear response (within the limitations of the photodiode) and increasing the power to the ± 1 - 10 V range. A 300 MΩ resistor, a 1μF capacitor, and an operational amplifier were used in the circuit for the photodiode detector.

The slow response detector was not as successful as planned, but nonetheless, improved experimental response. The expectation was that the measured fluctuations in laser power would correlate to the noise in the experimental signals. This was not observed, but the slow response detector reduced the noise of a simple pump-probe signal by an order of magnitude. It did not reduce the noise of the MUPPETS experiment, but it did correct for long term power fluctuations in a single data collection period and adjusted the signal for power fluctuations across multiple data collection periods. The lack of noise reduction in MUPPTES signals is likely due to the fact phase noise is the primary source of noise and not pulse-to-pulse fluctuations in laser power.

2.6.2 Double Modulation

The MUPPETS theory, as shown in Figure 1.1, suggests that the signal detected will only be from molecules that interacted with each of the first two pulse pairs. In reality, signals from 2, 3, or 4 beam combinations also contribute to the MUPPETS signal. These background signals can be accounted for if they remain constant and are small relative to the desired signal; however, this was not always the case. The size of the background signals were sometimes large in comparison to the MUPPETS signal and the size varied

during the course of experiments. An example of variations in the background signal is shown in figure 2.6. The variation in the noise levels during the course of an experiment could not be correlated to a known cause.

A double modulation scheme was introduced to eliminate background signals from the MUPPETS signals. Prior to double modulation, a single laser pulse (1c) was chopped at 500 Hz. The remaining five pulses had a frequency of 1000 Hz. In the double modulation scheme, the original chopper remained in pulse 1c, but the frequency was reduced to 250 Hz. A second chopper was introduced in the delay line region; thus, pulses 2a and 2b were chopped. The frequency of the second chopper was also 250 Hz but at a 90° phase shift. In the double modulation scheme, all three pulse pairs only overlapped once every pulse cycle and the detection of background signals caused by other pulse combinations is undetectable. This, however, reduced the signal size by a factor of two. The signal size was artificially increased by replacing the resistor and capacitors in the RC circuits of PD1 and PD2. Since V = IR, increasing the resistance of the resistor by a factor of 10 increases the voltage of the signal by a factor of 10. The response of the circuit was kept constant by reducing the capacitance of the capacitor by a factor of 10. The change in the RC circuit increase the signal and the noise by a factor of 10. The change was made to increase the signal size on the lock-in amplifier. This was not a necessary change, but it is beneficial to the researcher when the signal sizes are not near the minimum detection level of the detection system.

2.6.3 Addition of Optical Elements and other Considerations

Additional optics were also added to the MUPPETS optical assembly to increase the capabilities of the optical assembly. On the ultrafast timescale, the travel time of a laser

pulse varies depending on the thickness of the lens. The varying change in travel time is accounted for by the addition of silicon windows that we refer to as timing plates. When a timing plate is tilted at the appropriate angle, a pulse that travels through the thinner edge of a lens and the timing plate will experience the same decrease in travel time as a pulse that travels through the thicker center of the lens. In previous versions of MUPPETS, the timing plate in pulse 3c was fixed to a mount that contained double differential micrometer. The differential micrometer is used to adjust the phase of one pulse pair relative to the other two pulse pairs. Phase control was added to the timing plates in pulses 1c and 2b.

The alignment of the delay lines was imperfect in previous versions of MUPPETS. A horizontal displacement was seen at the sample position after the delay line was put into place. The prisms used to steer the beams into the delay lines were likely not manufactured at perfect 90° angle. The delay line for pulses 2 and 3 contain a right angle change in the optical plane to save space on the optical table. Previous versions of MUPPETS used a single mirror for the outbound and return path of each pulse. A second mirror was added to the return path to correct horizontal displacements in the delay line alignment.

The power of the femtosecond pulse on G1 must be monitored. At powers greater than ~10 mW, self-focusing can occur inside of the grating. Self focusing is a non-linear optical effect caused by changes in the refractive index of material due to high intensities of electromagnetic radiation. Self-focusing occurs in G1 when the radiant exposure is in the range of $1 \cdot 10^{15}$ $J \cdot m^{-2}$. Figure 2.7a displays an image of pulse 2b when non-linear optical effects occur at G1. Figure 2.7b displays an image of pulse 2b when non-linear effects do not occur at G1. Figure 2.7c displays cross sections of each image. When self-

focusing occurs, the MUPPETS signal does not increase as the power increases. The signal to noise ratio increases as well.

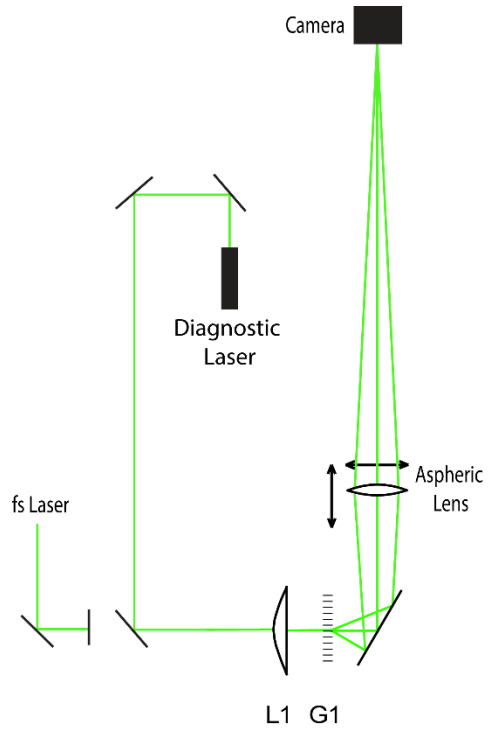

Figure 2.1 A schematic of the diagnostic microscope setup.

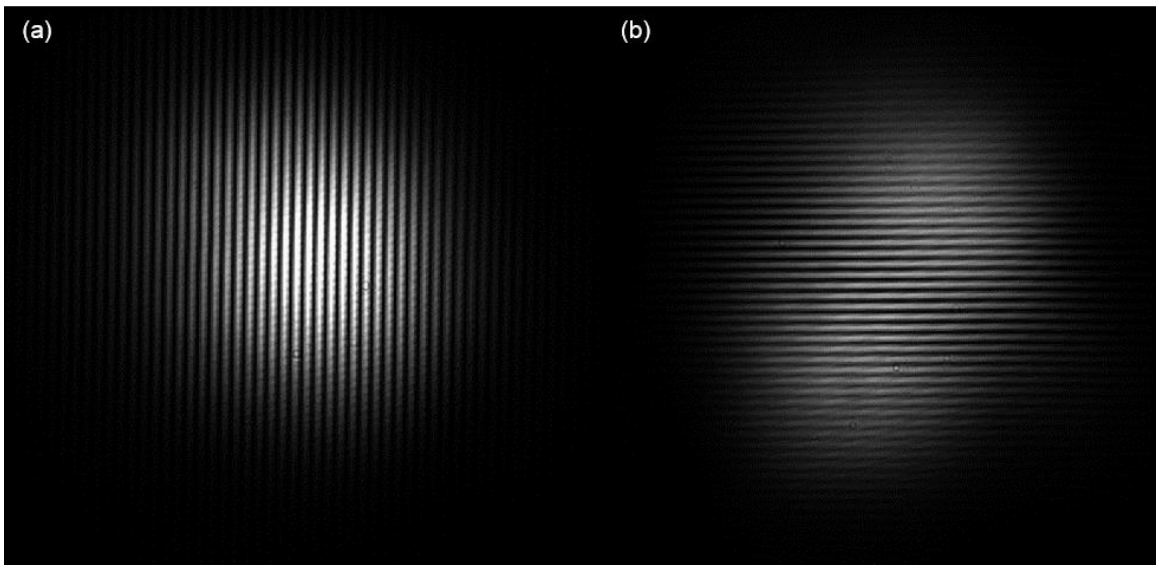

Figure 2.2 An example of astigmatism is shown at G2. (a) Beams 3a and 3c, sagittal plane, viewed at their focal point. (b) Beams 1b and 2b, tangential plane, viewed at the focal point of 3a and 3c. They possess a different focal point, i.e. an astigmatism.

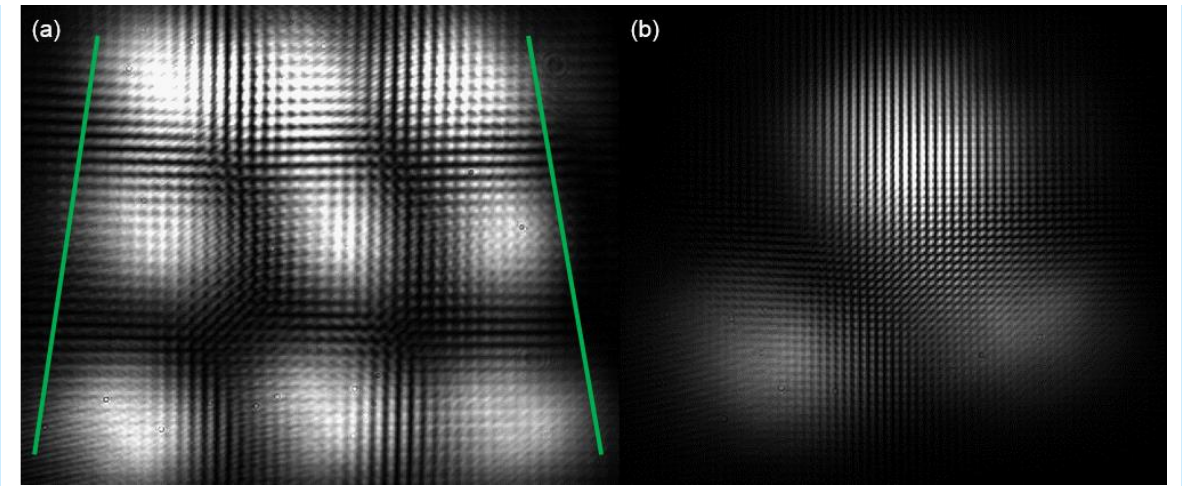

Figure 2.3 (a) Coma viewed 4 mm before the focal point of the MUPPETS optical assembly caused by a 1° tilt about the y-axis in L5. Green lines emphasize the effect of coma (b) Coma viewed at the focal point of beams 2a and 2c caused by a 2° tilt about the y-axis in L5. It is shown that 1a and 1c possess a different focal point.

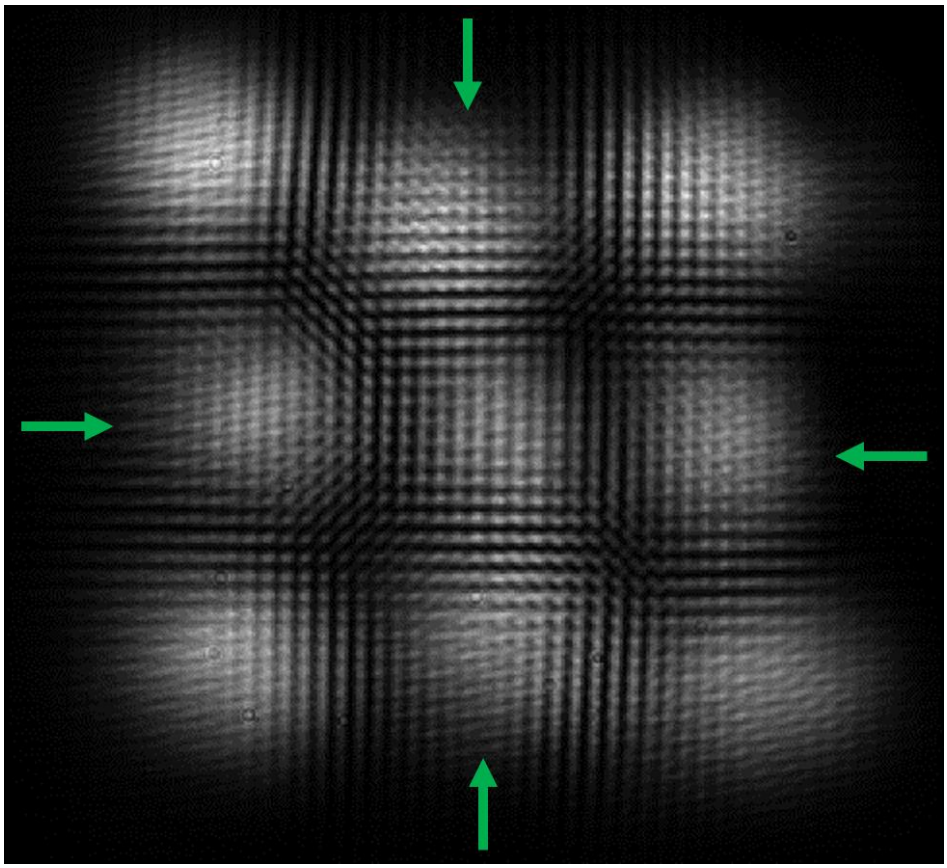

Figure 2.4 Spherical aberration caused by a −1 mm translation about the z-axis of ML2 is shown 4 mm before the focal point of the MUPPETS optical assembly. Green arrows emphasize the effect of spherical aberration.

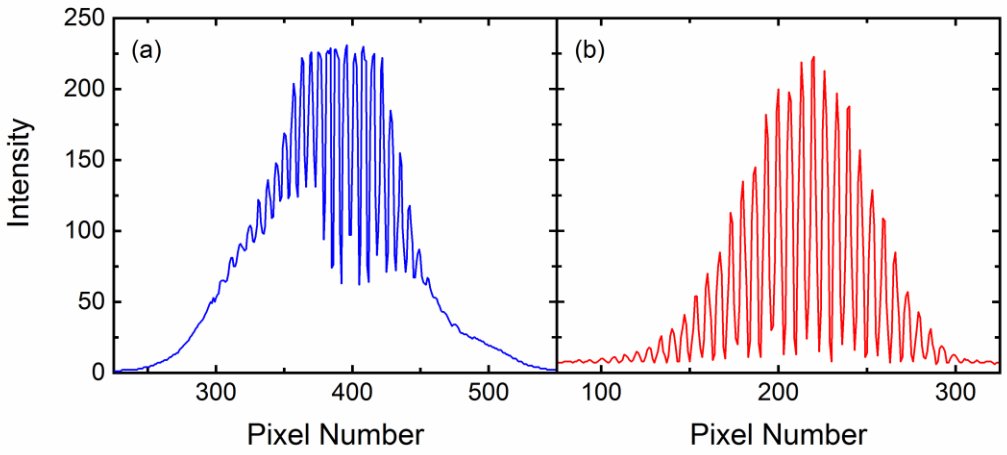

Figure 2.5 (a) Cross section obtained from an image of beams 3a and 3c that possess optical aberrations. (b) Cross section obtained from an image of beams 1 and 2 at G2 that are free of optical aberrations.

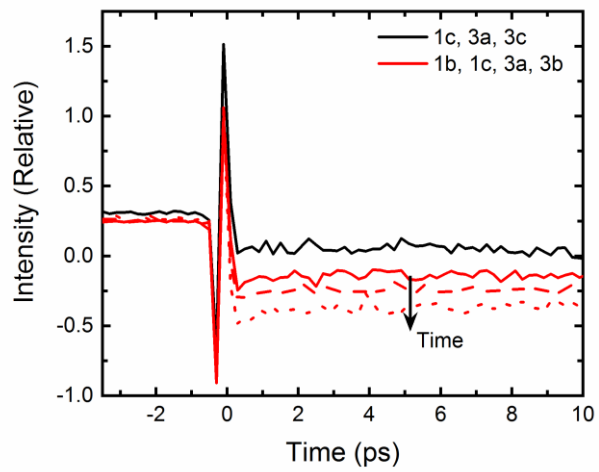

Figure 2.6 Background signals for pulse combination 1c, 3a, and 3c (black) and pulse combination 1b, 1c, 3a, and 3c (red). Pulse combination 1b, 1c, 3a, and 3c display changes in the background signal over time. Solid red represents early times, dashed red line represents medium time, and the dotted red line represents long time. The range of time covers the duration of a MUPPETS experiment. The signal size at negative times, caused by scattered light, remained constant indicating no substantial change in the laser power.

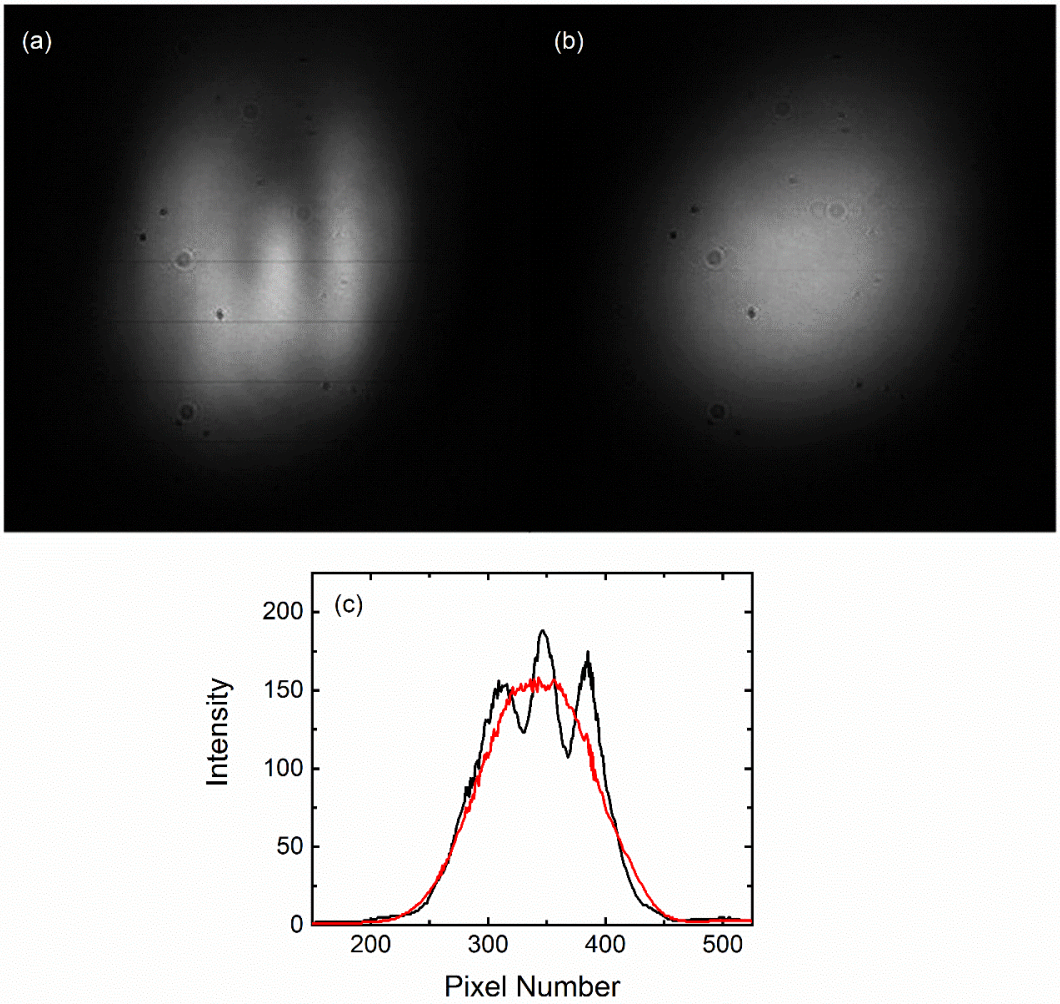

Figure 2.7 Non-linear effects in G1 caused by high power is shown. (a) Pulse 3b at maximum laser power. (b) Pulse 3b at reduced laser power. (c) Horizontal cross sections of 2.7a and 2.7b.

CHAPTER 3

MEASURING A HIDDEN COORDINATE: RATE-EXCHANGE KINETICS FROM 3D CORRELATION FUNCTIONS[1]

[1] Reproduced from Mark A. Berg and Jason R. Darvin *J. Chem. Phys.* **2016**, *145*, 054119 with the permission of AIP Publishing

3.1 Introduction

Rate dispersion—nonexponential relaxation—occurs in a wide variety of systems. Notable examples are supercooled liquids,[1-7] polymers,[8-12] biomolecules,[13-19] ionic liquids,[20-25] and nanoparticles.[26-32] The absence of rate dispersion in simpler materials is easy to explain. Exponential relaxation with a single rate implies that the surroundings hold no long-term memory about the process being observed; the system is Markovian. Conversely, rate dispersion indicates a non-Markovian system and demands some "hidden coordinate" that retains memory of the past.[33] The ultimate goal is to identify the physical process represented by the hidden coordinate. The proximate problem is to measure the properties of the hidden process, even though it is not directly observable. This paper tackles the latter issue. It uses a general model to show how the kinetics of the hidden variable associated with heterogeneous rate dispersion can be measured from a 3D correlation function. Standard kinetics are based on one dimensional (1D) measurements—experiments that monitor the system's evolution over one time interval. They measure the mean rate and the total size of the rate dispersion from all sources, but nothing more. In particular, they do not distinguish between homogeneous and heterogeneous contributions to rate dispersion. When every molecule has the same nonexponential decay, the dispersion is homogeneous. When different subensembles of molecules having distinguishable dynamics, the dispersion is heterogeneous.

Two dimensional (2D) measurements—those that include evolution over two time intervals—offer more. Previous work has already shown that 2D response functions yield the fraction of the rate dispersion that is due to heterogeneity.[34,35] This paper will extend those conclusions to correlation functions. In the case of rate heterogeneity, the

environmental factors that change the dynamics of different molecules are the hidden process, and the mean rate of a subensemble can be used as the hidden coordinate. Thus, 2D measurements are a route to learning about the probability distribution of this hidden coordinate.

Questions remain. In systems that equilibrate and are ergodic, a single molecule must eventually move through all the rate ensembles. In addition to the kinetics of the observable, we also want to know the dynamics of exchange between environments: What is the mean exchange time? Is the exchange Markovian and single exponential, or does it also show dispersed relaxation?

Many methods have been proposed to gain more information about complex kinetics from a time series of observations: hidden Markov models,[36-39] constrained 1D correlation functions,[40,41] two-event correlation functions,[42] multipoint correlations,[3] and time windowed correlation functions.[4] We recently summarized the advantages of multidimensional correlation functions, the method pursued here.[7] Such functions have been calculated for specific systems by a number of groups.[7,25,43-67] Often, these studies analyzed simulation data and have recognized that three dimensional (3D) correlation functions should be sensitive to rate exchange.[25,53-66] More recently, 3D correlation functions have been applied to single-molecule data.[7,67] In all these papers, the connection between 3D correlation functions and rate exchange has been argued at a qualitative level, and the quantification of the exchange dynamics has been through ad hoc measures.

The main purpose of this paper is to provide rigor for the connection between 3D correlation functions and rate exchange. To accomplish this task, a model is developed that is both general enough to approximate many real systems, but is also simple enough

to calculate multidimensional correlation functions. This "slow heterogeneity" model contains both homogeneous and heterogeneous contributions to rate dispersion. It also includes exchange between rate subensembles, but the exchange is slow relative to the decay of the observable. Two variations of this model are possible, one where the observable jumps random distances within its distribution and one where only small steps are made. Within this model, well-defined measures of the dynamics of the hidden coordinate governing rate exchange can be extracted from 3D correlation functions.

In addition to this intended result, we also come to two unanticipated conclusions. First, the 3D correlation function contains two contributions, one that reports on the dynamics of the exchange process and another that does not. A similar thing happens in multidimensional spectroscopy: a single measurement is a sum of different "pathways," different terms representing different dynamical behavior.[68] The weighting of these terms is not universal; it depends on the shape of the distribution of the observable. Extracting an uncontaminated measurement of the exchange kinetics in the face of these issues is a challenge. Some simple approaches are discussed here. More sophisticated ones will be presented in the future,[69] but they build on the model developed in this paper.

The second idea that emerges is a new perspective on the role of multidimensional correlation functions. Static (0D) statistics and 1D correlation functions define the distribution and kinetics of an observed quantity. If rate dispersion is found, a hidden process is implied. Two- and three-dimensional correlation functions report on the distribution and kinetics of the corresponding hidden coordinate. If these kinetics are dispersed, a second level of hidden dynamics is implied. Higher dimensional correlation functions probe increasingly deep into this hierarchy.

3.2 Defining the Slow Heterogeneity Model

Assume that an observable property $X(t)$ undergoes spontaneous fluctuations at equilibrium. The N-dimensional correlation function $C_X^{(N)}(\tau_N,\ldots,\tau_1)$ is defined by

$$C_X^{(N)}(\tau_N,\ldots,\tau_1)=\frac{\langle X(t_N)\ldots X(t_1)X(t_0)\rangle}{\langle X^2\rangle^{(N+1)/2}} \tag{1}$$

where the brackets indicate an ensemble average. The system is ergodic, so either a time average over t_0 or an average over multiple molecules can be used.[7] The observable $X(t)$ is defined so its mean is zero, $\langle X\rangle = 0$. Absolute times t_i and time intervals $\tau_i = t_i - t_{i-1}$ will be used interchangeably to simplify the notation. The normalization factor makes the 1D function one at time zero. Higher correlation functions have an initial amplitude relative to the 1D function.

In addition to the observable, there is another slow variable $\theta(t)$ that cannot be measured directly. At equilibrium, the joint probability of these variables is $P(X_0, \theta_0)$. The time evolution of the system is governed by a stationary Green's function (conditional probability) $G(X_1, \theta_1 \mid X_0, \theta_0; t_1 - t_0)$. The correlation functions can be rewritten with the time dependence shifted to this function:

$$\begin{aligned} C^{(N)}(\tau_N,\ldots,\tau_1) = \langle X^2\rangle^{-(N+1)/2} & \iint dX_N d\theta_N \; X_N \\ & \times\left(\prod_{i=0}^{N-1}\iint dX_i d\theta_i \; G(X_{i+1},\theta_{i+1} \mid X_i,\theta_i;t_{i+1}-t_i)X_i\right) \\ & \times P(X_0,\theta_0) \end{aligned} \tag{2}$$

From right to left, the initial, equilibrium distribution $P(X_0, \theta_0)$ is multiplied by X_0 to measure the observable at t_0. The system is propagated to t_1 by the Green's function and the integration over X_0 and θ_0. Measurement and propagation are repeated N times. A final measurement comes from multiplying by X_N, and the ensemble average is accomplished by the integrals over X_N and θ_N.

From this general expression, the slow heterogeneity model is built from several assumptions. The observable and hidden variable are taken to be uncorrelated at equilibrium,

$$P(X,\theta) = P_X(X)P_\theta(\theta), \tag{3}$$

where $P_X(X)$ is the equilibrium distribution of $X(t)$, and $P_\theta(\theta)$ is the equilibrium distribution of $\theta(t)$. From the assumption that $X(t)$ has a mean of zero, we have

$$\int_{-\infty}^{\infty} dX \; XP_X(X) = 0. \tag{4}$$

The time evolution of the system is assumed to obey

$$\begin{aligned} G(X_{i+1},\theta_{i+1} \mid X_i,\theta_i;\tau_{i+1}) = G_X(X_{i+1} \mid X_i;\tau_{i+1}/\theta_i) \\ \times G_\theta(\theta_{i+1} \mid \theta_i;\tau_{i+1}) \end{aligned}. \tag{5}$$

The evolution of the observable is given by $G_X(X_{i+1} \mid X_i;\ \tau_{i+1}/\theta_i)$, and that of the hidden coordinate is governed by $G_\theta(\theta_{i+1} \mid \theta_i;\ \tau_{i+1})$. Equation 5 specifies that the evolution of the hidden coordinate $\theta(t)$ is unaffected by the observable $X(t)$. The evolution of $X(t)$ is only coupled to $\theta(t)$ by a uniform expansion or contraction of its decay profile. All the subensembles have the same decay shape; only their mean decay times differ. In addition,

the evolution of $\theta(t)$ is slow relative to the equilibration of $X(t)$, so the initial value of $\theta(t)$ governs the evolution of $X(t)$ over its entire decay.

The standard measurement of dynamics is the 1D correlation function,

$$C_X^{(1)}(\tau_1) = \frac{\langle X(\tau_1)X(0)\rangle}{\langle X^2\rangle}. \tag{6}$$

The assumptions made so far reduce Equation 2 to

$$C_X^{(1)}(\tau_1) = \int_0^\infty d\theta\, g(\tau_1/\theta)P_\theta(\theta). \tag{7}$$

where

$$g(x) = \int_{-\infty}^{\infty}\int_{-\infty}^{\infty} dX_1 dX_0\; X_1 G_X(X_1 \mid X_0; x) X_0 P_X(X_0). \tag{8}$$

The homogeneous decay $g(\tau/\theta)$ is the decay of a subensemble of molecules with a fixed value of $\theta(t)$. Equation 6 has been widely used to describe how the total observed rate dispersion arises from a combination of heterogeneous rate dispersion, which comes from the width of $P_\theta(\theta)$, and homogeneous rate dispersion, which comes from a nonexponential $g(x)$. For our purposes, note that all information on the dynamics of $\theta(t)$ is lost. A static heterogeneity and one undergoing slow exchange are indistinguishable. Information on $P_\theta(\theta)$ survives, but it is impossible to deconvolve from $g(x)$.

To move to higher correlation functions, additional assumptions will be needed. First note that with slow exchange, the following approximation is good:

$$G_\theta(\theta_{i+1} \mid \theta_i; \tau_{i+1}) g(\tau_{i+1}/\theta_i) \approx \delta(\theta_{i+1} - \theta_i) g(\tau_{i+1}/\theta_i). \tag{9}$$

The observable relaxes completely before $\theta(t)$ changes. We also need more information about $G_X(X_{i+1} \mid X_i;\ \tau_{i+1}/\theta_i)$. In general, the dynamics of the observable could vary with position in the distribution. Only one type of average over position is given by $g(x)$ [Equation 8]. The model is restricted to cases where this average alone is sufficient to specify the homogeneous decay of individual subensembles.

Two cases are consistent with this restriction. The first, "strong"-relaxation case is defined by

$$G_X(X_{i+1} \mid X_i; x) = g(x)\delta(X_{i+1} - X_i) + \big(1 - g(x)\big)P_X(X_{i+1}) \tag{10}$$

The value of $X(t)$ remains fixed at a single value [the first term in Equation 10] until an event scatters it to a random position within the equilibrium distribution [the second term in Equation 10]. This model accommodates any distribution for the observable: Gaussian or not, symmetric or asymmetric, discrete or continuous. It includes the important case of a two-level system.

The second case has "weak" relaxation in which the observable only moves by small steps. It is necessary to have a Gaussian distribution of the observable,

$$P_X(X) = \frac{1}{\sqrt{2\pi}\sigma}\exp\left(-\frac{X^2}{2\sigma^2}\right). \tag{11}$$

It is not necessary that the original experimental quantity be Gaussian. Any continuous distribution can be changed to this shape by a transformation of variables. The important assumption is that after this transformation, it has Gaussian dynamics within each subensemble[70]

$$G_X(X_1 \mid X_0; x) = \frac{1}{\sqrt{2\pi\left(1-g(x)^2\right)}\,\sigma} \exp\left[-\frac{\left(X_1 - g(x)X_0\right)^2}{2\sigma^2\left(1-g(x)^2\right)}\right]. \quad (12)$$

Note that the ensemble distribution is not Gaussian during relaxation. These dynamics are diffusive and allow for a time dependent diffusion constant. However, the diffusion constant must be uniform across the distribution. The assumption of a uniform diffusion constant differs from the assumption of a uniform residence time, which defines strong relaxation.

The model defined by these assumptions is relatively general. Any distribution of $\theta(t)$ can be treated. Both the homogeneous decay $g(x)$ and the exchange process $G_\theta(\theta_1 \mid \theta_0; \tau_1)$ may be exponential or not. This flexibility is balance by simplicity. The model is defined by a small number of uncoupled functions: $P_X(X)$ and $g(x)$ describe the equilibrium and time-dependent properties of the observable; $P_\theta(\theta)$ and $G_\theta(\theta_1 \mid \theta_0; \tau_1)$ do the same for the hidden variable. This balance is a good match for many experimental systems, for example, supercooled liquids and polymers.[4-7,58-60]

If $g(x)$ is non-exponential, in other words, if there is homogeneous rate dispersion, it must be caused by a different hidden variable $\varphi(t)$. An average over the dynamics of $\varphi(t)$ is implicit in $g(x)$ [Equation (8)]. The variable that we are concerned with $\theta(t)$ is distinguished from $\varphi(t)$ by its lack of correlation with the observable: $\theta(t)$ is uncorrelated from $X(t)$ at equilibrium [Equation (3)], and because $G_\theta(\theta_1|\theta_0; \tau_1)$ is independent of $X(t)$, correlations do not build with time. The same is not true of $\varphi(t)$. This point will be elaborated in the future. Here we simply point out that our conclusions only pertain to a hidden coordinate associated with rate heterogeneity.

3.3 Strong Relaxation Model

The weak relaxation model will be considered in Section 3.6 We first look at multidimensional correlation functions for the strong relaxation model, which has simpler results. Using Equations 2 and 5 along with Equation 10, calculations are straightforward for correlation functions with successively higher dimensions. Because Equation 10 contains two terms in the time evolution, the number of terms doubles with each additional dimension. Fortunately, many terms are eliminated by Equation 4. Initially, each term also contains $N + 1$ integrals over θ_i's. The assumption of slow exchange [Equation 9] reduces the number greatly.

The 2D correlation function,

$$C_X^{(2)}(\tau_2,\tau_1)=\frac{\langle X(\tau_2+\tau_1)X(\tau_1)X(0)\rangle}{\langle X^2\rangle^{3/2}}, \tag{13}$$

becomes

$$C_X^{(2)}(\tau_2,\tau_1)=\beta_1\int_0^\infty d\theta\, g(\tau_2/\theta)g(\tau_1/\theta)P_\theta(\theta). \tag{14}$$

The amplitude of the correlation function is determined by the distribution of the observable through the parameter β_1,

$$\beta_1=\frac{\langle X^3\rangle}{\langle X^2\rangle^{3/2}}, \tag{15}$$

the skewness of the distribution.[71] The distribution of the observable is irrelevant to the 1D correlation function. Equation 14 is the first example of the distribution playing a role in a higher correlation function. For 2D, the most important effect is that the amplitude is

zero for a symmetric distribution. (Section 3.7 will give a work-around for such systems.) Although the same functions appear in the 1D expression [Equation 7], the integral in Equation 14 can be uniquely decomposed into $g(x)$ and $P_\theta(\theta)$. This result has been worked out in the context of 2D response functions.[34] However, the same integral appears for response functions and correlation functions, so there is no need to repeat the reasoning here. The important point is that the 2D correlation function yields the distribution of the hidden variable $P_\theta(\theta)$, but no information on its dynamics.

The focus of this paper is the 3D correlation function,

$$C_X^{(3)}(\tau_3,\tau_2,\tau_1)=\frac{\left\langle X(\tau_3+\tau_2+\tau_1)X(\tau_2+\tau_1)X(\tau_1)X(0)\right\rangle}{\left\langle X^2\right\rangle^2}. \qquad (16)$$

For the first time, multiple terms survive:

$$C_X^{(3)}(\tau_3,\tau_2,\tau_1)=(\beta_2-1)C_{f1}^{(3)}(\tau_3,\tau_2,\tau_1)+C_{\mathrm{ex}}^{(3)}(\tau_3,\tau_2,\tau_1). \qquad (17)$$

We denote the terms $C_{f1}^{(3)}(\tau_3,\tau_2,\tau_1)$ (filter 1) and $C_{\mathrm{ex}}^{(3)}(\tau_3,\tau_2,\tau_1)$ (exchange) for reasons that will become clear. Each is normalized to one at the overall time origin. Their relative contributions depend on the shape of $P_X(X)$ through β_2, the ratio of fourth to second moments,

$$\beta_2=\frac{\left\langle X^4\right\rangle}{\left\langle X^2\right\rangle^2}, \qquad (1)$$

the kurtosis of the distribution.[71] The problem simplifies to a single term only if $\beta_2 = 1$, for example, a two-level system with equal populations. Any other distribution combines the

two terms with a distribution-specific weighting. For example, a Gaussian has $\beta_2 = 3$, and both terms are significant: $C^{(3)} = 2C_{f1}^{(3)} + C_{\text{ex}}^{(3)}$.

The relative weighting is important, because each term has a different behavior during τ_2. The filter 1 term,

$$C_{f1}^{(3)}(\tau_3, \tau_2, \tau_1) = \int_0^\infty d\theta \; g(\tau_3 / \theta) g(\tau_2 / \theta) g(\tau_1 / \theta) P_\theta(\theta), \tag{19}$$

follows the pattern of the 1D and 2D correlation functions [Equations 7 and 13]. Its behavior can be understood by writing it as

$$C_{f1}^{(3)}(\tau_3, \tau_1; \tau_2) = C^{(1)}(\tau_2) \int_0^\infty d\theta \; g(\tau_3 / \theta) g(\tau_1 / \theta) P_{f1}(\theta; \tau_2) \tag{20}$$

This term now appears to be a pseudo-2D correlation function at each value of τ_2 [compare to Equation 14]. The difference from the true 2D function is that the true distribution $P(\theta)$ has been replaced with a modified, pseudo-probability distribution $P_{f1}(\theta; \tau_2)$,

$$P_{f1}(\theta; \tau_2) = \frac{g(\tau_2 / \theta) P_\theta(\theta)}{C^{(1)}(\tau_2)}. \tag{21}$$

This distribution is normalized for all τ_2. The contribution of the faster subensembles (those with smaller θ's) is reduced by the factor of $g(\tau_2 / \theta)$; they have been "filtered" out of the distribution. Significantly, $G_\theta(\theta_3 | \theta_1; \tau_2)$ does not appear in Equation 20. This term has no information about rate exchange.

In contrast, the second term in Equation 17has a decay during τ_2 that is solely due to rate exchange:

$$C_{\mathrm{ex}}^{(3)}(\tau_3,\tau_2,\tau_1)=\int_0^\infty\int_0^\infty d\theta_3 d\theta_1\; g(\tau_3/\theta_3)G_\theta(\theta_3\,|\,\theta_1;\tau_2)$$
$$\times g(\tau_1/\theta_1)P_\theta(\theta_1) \qquad . \qquad (22)$$

The first problem is how to isolate information about $G_\theta(\theta_3\,|\,\theta_1;\,\tau_2)$ from this term. The second is how to isolate the exchange term's contribution to the total, measured $C^{(3)}(\tau_3,\,\tau_2,\,\tau_1)$.

3.4 Extracting a Correlation Function of the Hidden Variable

Information about Gθ(θ3 | θ1; τ2) will come most easily in the form of $C_\theta^{(1)}(\tau)$, a 1D correlation function of the hidden variable,

$$C_\theta^{(1)}(\tau)=\frac{\langle\delta\theta(\tau)\delta\theta(0)\rangle}{\langle\delta\theta^2\rangle}\quad, \qquad (23)$$

with $\delta\theta(\tau) = \theta(\tau) - \square\theta\square$ [compare to Equation 6]. This expression can also be written in terms of the Green's function of the hidden variable:

$$C_\theta^{(1)}(\tau)=\int_0^\infty\int_0^\infty d\theta_3 d\theta_1\;\delta\theta_3 G_\theta(\theta_3\,|\,\theta_1;\tau)\delta\theta_1 P_\theta(\theta_1)\quad. \qquad (24)$$

It will be convenient to define a functional $Q_{31}[f](\tau_2)$ that integrates over τ_3 and τ_1,

$$Q_{31}[f](\tau_2)=\int_0^\infty\int_0^\infty d\tau_3 d\tau_1\; f(\tau_3,\tau_2,\tau_1)\quad. \qquad (25)$$

If $C_{\mathrm{ex}}^{(3)}(\tau_3,\tau_2,\tau_1)$ is integrated, the correlation decay of $\theta(t)$ emerges:[58-62]

$$Q_{31}[C_{\mathrm{ex}}^{(3)}](\tau_2)=\langle\delta\theta^2\rangle C_\theta^{(1)}(\tau_2)+\langle\theta\rangle^2\quad. \qquad (26)$$

In a future paper, we will argue that a different measure has advantages,[69] but Equation 26 makes the main point. Extracting a well-defined measure of the kinetics of the hidden variable from the exchange term is straightforward.

Unfortunately, integrating the measured 3D correlation function gives a more complex expression,

$$Q_{31}[C_X^{(3)}](\tau_2) = \left\langle \delta\theta^2 \right\rangle C_\theta^{(1)}(\tau_2) + \langle\theta\rangle^2 + (\beta_2 - 1) C_X^{(1)}(\tau_2) \int_0^\infty d\theta\, \theta^2 P_{f1}(\theta;\tau_2) \quad . \tag{27}$$

The integral in this expression does not simplify in general. For a specific system, full analysis of the 2D correlation function should yield both $g(x)$ and $P_\theta(\theta)$. With these functions, $P_{f1}(\theta;\tau_2)$ and its integral can be calculated, and the exchange-correlation function can be extracted. Another approach is to note that the last term in Equation 27 decays with $C_X^{(1)}(\tau_2)$. If $\bar{T}$, the decay time of the observable, is sufficiently well separated from the exchange time T_{ex}, one can simply ignore the early data to obtain the exchange kinetics:

$$\frac{Q_{31}[C_X^{(3)}](\tau_2) - Q_{31}[C_X^{(3)}](\infty)}{Q_{31}[C_X^{(3)}](\tau_2{}^*) - Q_{31}[C_X^{(3)}](\infty)} \xrightarrow[\tau_2 \geq \tau_2{}^*]{\bar{T} \ll \tau_2{}^* \ll T_{ex}} C_\theta^{(1)}(\tau_2) \quad . \tag{28}$$

Thus, the primary claim of the paper is established. The 1D dynamics of the hidden coordinate $\theta(t)$ can be obtained from the 3D dynamics of the observable $X(t)$. One can recover not just the mean exchange time, but the full shape of the exchange process, including any dispersion in the exchange rate.

3.5 3D Rate-Correlation Spectra

Although the last section showed that the kinetics of rate exchange can be measured in principle, the approaches to correcting for the filter term are demanding in practice. This section looks at the problem from the perspective of time-dependent (3D) rate-correlation spectra. These spectra are an extension of 2D (static) rate-correlation spectra[34,72] and mimic the time-dependent frequency-correlation spectra used in 3D coherence spectroscopy.[73,74] Time-dependent rate-correlation spectra are an intuitive way to present multidimensional kinetics and have appeared in recent publications.[25,62] They will suggest ways to improve the analysis of multidimensional kinetics.

The 3D rate-correlation spectrum $\hat{C}_X^{(3)}(y_3,\tau_2,y_1)$ is defined implicitly by

$$C_X^{(3)}(\tau_3,\tau_2,\tau_1)=\int_0^\infty\int_0^\infty dT_3 dT_1\,\hat{C}_X^{(3)}(y_3,\tau_2,y_1) \times\exp\left(-\tau_3/T_3\right)\exp\left(-\tau_1/T_1\right) . \tag{29}$$

with

$$y_i=\log_{10}\frac{T_i}{\bar{T}} . \tag{30}$$

It involves a 2D inverse-Laplace transform from time intervals τ_i to time constants (inverse rates) T_i, along with a shift to a logarithmic scale y_i. The origin of this scale is set to $\bar{T}$, a time characteristic of the relaxation of $X(t)$.

To illustrate the behavior of this spectrum, we set up a simple example. The observable is distributed as a Gaussian (β_1 = 0, β_2 = 3) and has a biexponential homogeneous decay,

$$g(x) = \tfrac{1}{2}\left(e^{-x/2} + e^{-2x}\right). \tag{31}$$

with rates differing by a factor of four. In addition, it has five subensembles with rates also separated by factors of four,

$$P(\theta) = \tfrac{1}{12}\left(\delta(\theta - 16\bar{T}) + 3\delta(\theta - 4\bar{T}) + 4\delta(\theta - \bar{T}) + 3\delta(\theta - \bar{T}/4) + \delta(\theta - \bar{T}/16)\right). \tag{32}$$

The exchange time T_{ex} is taken to be the half-life of $C_{\theta}^{(1)}(\tau_2)$, which is much longer than $\bar{T}$. For reference, the homogeneous decay and the full 1D correlation function are compared to a single exponential in Figure 3.1. The increased spread of $g(\tau/\bar{T})$ (red) relative to the exponential (black) represents homogeneous rate dispersion. The even larger spread of $C_X^{(1)}(\tau_1)$ (blue) includes the additional effects of heterogeneous rate dispersion.

Rate-correlation spectra for this system are shown in Figure 3.2. (The exact results are a set of delta functions. They have been interpolated with a smooth surface to make contour plots.) The individual contributions, $\hat{C}_{ex}^{(3)}(y_3, \tau_2, y_1)$ and $\hat{C}_{f1}^{(3)}(y_3, \tau_2, y_1)$, are shown in the top and middle rows, respectively. The measured result $\hat{C}_X^{(3)}(y_3, \tau_2, y_1)$ is the weighted sum of these two [Equations 17] and is shown in the bottom row.

In the left-hand column, $\tau_2 = 0$, and no exchange or filtering has occurred. The two components (and thus the total) have identical shapes. These spectra are equivalent to a 2D measurement (see Section 3.7). The width along the anti-diagonal ($y_1 = -y_3$) is only due to homogeneous dispersion, whereas the width along the diagonal ($y_1 = y_3$) includes the heterogeneous dispersion. Thus, the elongation of the peak indicates the fraction of the dispersion due to heterogeneity.

In the next two columns (τ_2 = $\bar{T}$ and $4\bar{T}$), τ_2 passes through the decay of the observable. Because exchange is slow on this scale, $\hat{C}^{(3)}_{\mathrm{ex}}(y_3,\tau_2,y_1)$ does not change. Over the same period, $\hat{C}^{(3)}_{f1}(y_3,\tau_2,y_1)$ decreases in amplitude, shifts toward longer time constants, and becomes less elongated. All three effects can be interpreted as filtering of the heterogeneous distribution. As fast subensembles are removed, the size of the correlation function drops, the average shifts toward slower times, and the remaining distribution narrows. The observed spectra (bottom row) combine the unchanging exchange term and the shifting filtered term. The overall volume drops. The peak moves and the diagonal width varies, both non-monotonically. None of these changes are related to exchange kinetics.

In the last two columns of Figure 3.2 (τ_2 = T_{ex} and ∞), the decay of the observable is complete, and $\hat{C}^{(3)}_{f1}(y_3,\tau_2,y_1)$ no longer contributes. As rate exchange proceeds, $\hat{C}^{(3)}_{\mathrm{ex}}(y_3,\tau_2,y_1)$ changes. Its peak drops, it broadens along the anti-diagonal, and it contracts along the diagonal. The elongation characteristic of heterogeneity is lost. Rate exchange causes the system to appear homogeneous, even though heterogeneity exists.

This example gives a visual sense of the important contributions of the filtering term to the 3D correlation function. The method used to quantify the spectrum; volume, height, widths of cuts or projections, and so on; will determine whether this term contaminates an attempt to measure the exchange dynamics. When the time scales of observable relaxation and exchange are unambiguously different, it is enough to separate the early and late dynamics. When these time scales are less distinct, intermingling of these effects is possible.

All of these effects were seen in our recent study of solvation in an ionic liquid.[25] The peak due to diffusive solvation shifted to longer times, narrowed along the diagonal and broadened along the antidiagonal. In that system, the exchange dynamics overlap strongly with the diffusive solvation times. The measure used for the exchange dynamics would be sensitive to changes in width along the diagonal, and the filtering term may have contributed to the reported results. However, the effects are unlikely to be large enough to change the main conclusion that exchange occurs on a timescale similar to the diffusive solvation in that system.

The example in Figure 3.2 suggests that methods are possible that would be insensitive to the filter term. The exchange term $\hat{C}^{(3)}_{\mathrm{ex}}(y_3,\tau_2,y_1)$ increases its width along the antidiagonal axis, whereas the filtering term $\hat{C}^{(3)}_{f}(y_3,\tau_2,y_1)$ shifts and narrows only along the diagonal axis. A forthcoming series of papers will show that these effects are general and will develop methods for analyzing multidimensional data that discriminate between exchange and filter effects in 3D data.[69]

3.6 Weak Relaxation Model

The results from the weak relaxation model are similar to those with strong relaxation in many ways. Combining Equations 2–5 along with Equation 12 again allows straightforward calculations in which the number of terms increases with the number of dimensions. For the 2D correlation function, all the terms are zero, because the distribution is symmetric. (See Section 3.7 for further discussion of this problem.)

To present the 3D results, a modified filter term $C^{(3)}_{f2}(\tau_3,\tau_2,\tau_1)$, is needed,

$$C_{f2}^{(3)}(\tau_3,\tau_1;\tau_2)=C^{(1)}(\tau_2)\int_0^\infty d\theta\, g(\tau_3/\theta)g(\tau_1/\theta)P_{f2}(\theta;\tau_2)\,. \tag{33}$$

with

$$P_{f2}(\theta;\tau_2)=\frac{g^2(\tau_2/\theta)P_\theta(\theta)}{C^{(1)}(\tau_2)} \tag{34}$$

[compare to Equations 20 and 21]. The 3D correlation function becomes

$$C_X^{(3)}(\tau_3,\tau_2,\tau_1)=(\beta_2-1)C_{f2}^{(3)}(\tau_3,\tau_2,\tau_1)+C_{\text{ex}}^{(3)}(\tau_3,\tau_2,\tau_1)\,. \tag{35}$$

The fact that $\beta_2 = 3$ for this model has been used to make the correspondence to the strong relaxation result [Equation 17] clear. Other than the extra factor of $g(\tau_2/\theta)$ in the filter 2 term [Equation 34], the two models are identical. Unlike $P_{f1}(\theta;\ \tau_2)$, the normalization of $P_{f2}(\theta;\ \tau_2)$ changes with τ_2, but the effect on the observed correlation function is small.

Most important, the exchange-correlation function is unchanged and yields the correlation function of $\theta(t)$ by the methods described earlier. The filter 2 term $C_{f2}^{(3)}(\tau_3,\tau_2,\tau_1)$ can be explicitly modeled and subtracted, just as $C_{f1}^{(3)}(\tau_3,\tau_2,\tau_1)$ can. The filter 2 term decays in τ_2 on timescales that are similar to $C_X^{(1)}(\tau_2)$, so Equation 28 can be used for weak relaxation. Future work will show that $C_{f2}^{(3)}(\tau_3,\tau_2,\tau_1)$ has the same distinctive behavior that was seen in Figure 3.2 and that this behavior allows it to be excluded from a measurement of the exchange dynamics.[69]

3.7 Relationships between Correlation Functions

From their definitions alone [Equations 6, 13, and 16], it is not clear how 1D, 2D and 3D correlation functions are related. In the slow heterogeneity model, they are very simply connected. For either strong- or weak-relaxation cases, the 1D correlation is equivalent to cuts through the 3D correlation,

$$C_X^{(3)}(\tau_1,0,0)=\beta_2 C_X^{(1)}(\tau_1)=C_X^{(3)}(0,0,\tau_1). \tag{36}$$

If the 2D correlation exists ($\beta_1 \neq 0$), the $\tau_2 = 0$ slice of the 3D correlation is equal to the 2D correlation,

$$\beta_1 C_X^{(3)}(\tau_3,0,\tau_1)=\beta_2 C_X^{(2)}(\tau_3,\tau_1), \tag{37}$$

and the $\tau_1 = 0$ or $\tau_3 = 0$ slices of the 2D correlation are the same as the 1D correlation,

$$C_X^{(2)}(\tau_1,0)=\beta_1 C_X^{(1)}(\tau_1)=C_X^{(2)}(0,\tau_1). \tag{38}$$

For observables with symmetric distributions, the standard 2D correlation function $C_X^{(2)}(\tau_3,\tau_1)$ is unmeasurable. Equation 37 suggests that an alternative 2D correlation function $C_X^{(2')}(\tau_3,\tau_1)$ should be defined as the $\tau_2 = 0$ slice of the 3D correlation function,

$$C_X^{(2')}(\tau_3,\tau_1)=C_X^{(3)}(\tau_3,0,\tau_1), \tag{39}$$

or

$$C_X^{(2')}(\tau_3,\tau_1)=\frac{\left\langle X(\tau_3+\tau_1)X(\tau_1)^2X(0)\right\rangle}{\left\langle X^2\right\rangle^2}. \tag{40}$$

Compared to $C_X^{(2)}(\tau_3,\tau_1)$, only its amplitude is different; its dynamics are identical,

$$C_X^{(2')}(\tau_2,\tau_1)=\beta_2\int_0^\infty d\theta\, g(\tau_2/\theta)g(\tau_1/\theta)P_\theta(\theta) \tag{41}$$

[compare to Equation 14]. Equation 38 extends to the alternative correlation function,

$$C_X^{(2')}(\tau_1,0)=\beta_2 C_X^{(1)}(\tau_1)=C_X^{(2')}(0,\tau_1). \tag{42}$$

Thus, within the slow heterogeneity model, higher dimensionality correlation functions contain all the information in the lower ones. This property can be ascribed to the assumption that the dynamics are uniform across the distribution of the observable, either a uniform persistence time for strong relaxation or a uniform diffusion constant for weak relaxation. The model and this assumption can be tested by measuring different correlation functions and checking the validity of the relationships in this section.

One important cut of the 3D correlation function has not been discussed, and its form depends on whether the observable relaxation is strong or weak. In the strong relaxation model, the $\tau_1 = \tau_3 = 0$ cut is equal to the 1D correlation,

$$C_X^{(3)}(0,\tau_2,0)=\beta_2\int_0^\infty d\theta\, g(\tau_1/\theta)P_\theta(\theta)=\beta_2 C_X^{(1)}(\tau_2). \tag{43}$$

For the weak relaxation model, an extra factor of $g(\tau_2/\theta)$ enters:

$$C_X^{(3)}(0,\tau_2,0)=\beta_2\int_0^\infty d\theta\, g^2(\tau_2/\theta)P_\theta(\theta). \tag{44}$$

In the case of an exponential homogeneous decay and no heterogeneity, the decay times of these two cases differ by a factor of two. Thus, in many systems, this cut will be able to distinguish between strong and weak relaxation.

3.8 Response Functions Versus Correlation Functions

This paper has dealt solely with correlation functions calculated from the fluctuations of a system at equilibrium. For 1D kinetics, this correlation function is equivalent to the response function found by perturbing a system away from equilibrium and watching its return.[75] Kryvohuz and Mukamel have shown that for higher dimensions, the relationship between response functions and correlation functions becomes complex for a general dynamical system.[50,51] Nonetheless, the expression derived here for the 2D correlation function [Equation 14] has dynamics identical to those derived for a 2D response function within the same assumptions. [34,35] This simple relationship is an important result for the slow heterogeneity model.

Does the same simplicity extend to 3D? For a single observable system, it cannot. If an observable is perturbed and then returns to equilibrium, there is no place to store the information needed to measure a slow exchange time. However, it has been shown that in a two-observable system (molecular electronic state and orientation), a 3D response function can be measured that uses the slow observable to store rate information about the fast observable.[76] Response functions nearly identical to the correlation functions derived here are found, including the presence of two distinct terms. The question of which systems have simplified relationships between correlation and response functions occur merits further investigation.

3.9 Summary and Conclusions

Three-dimensional correlation functions are emerging as a systematic way to characterize rate exchange, both its mean time and its decay shape. This paper has introduced a simple and general model of rate heterogeneity that provides a quantitative

connection between the 3D correlation function and the correlation function of the variable associated with rate exchange. Systems that violate the restrictions of this model, for example with faster exchange[25] or kinetics that vary across the distribution,[51,52] may well be important. Nonetheless, the slow heterogeneity model developed here is a limiting case of this more complex behavior and will serve as a platform for building more elaborate models.

In the process of analyzing this model, we discovered that high dimensional correlation functions of incoherent kinetics are sums over multiple dynamical pathways. Within a pathway a specific dynamical process governs each time interval. Measurements cannot be automatically associated with a single processes; the contributions of the contributing pathways must be disentangled. The same situation exists in coherence spectroscopy[68] and in incoherent response functions.[76,77] In those areas, pathways can be associated with diagrams through the eigenstates of the system. A similar diagrammatic approach to incoherent, multidimensional correlation functions may be possible.

Extracting information on rate exchange from 3D correlation functions without contamination from a second, rate filtering pathway is a challenge. The methods suggested here are straightforward and demonstrate the feasibility of such separation. However, in a future series of papers, we will show that more sophisticated methods based on spectral transforms of the data provide a cleaner and more robust separation.[69]

Once these complications are taken into account, a 3D correlation function yields the full kinetics of rate exchange. The 2D correlation function provides the distribution of rates.[34] The 2D and 3D correlation functions characterize the hidden rate-exchange variable in the same way that the 0D statistics and 1D correlation function characterize the

observable. If the rate-exchange decay is non-exponential, and therefore non-Markovian, a second-level, even slower hidden coordinate is involved. Four- and five-dimensional correlation functions will characterize it, and so on through a potential hierarchy of processes. Ergodic systems have a maximum relaxation time scale, so this hierarchy will terminate when it reaches a Markovian variable with that time scale.

This scheme does not provide the specific physical mechanism that generates the hidden variable. Rather, it reduces a set of data to a set of statistical properties of that process. These properties provide the essential experimental constraints on specific physical models. Obtaining data to adequately characterize a deep hierarchy may be challenging, but the requirements are clear.

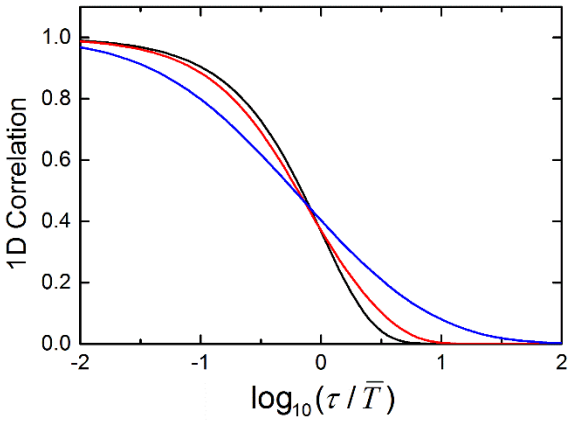

Figure 3.1 The 1D correlation function $C_X^{(1)}(\tau_1)$ of the system of Figure 3.2 (blue), its homogeneous component g($\tau/\bar{T}$) (red), and an exponential (black).

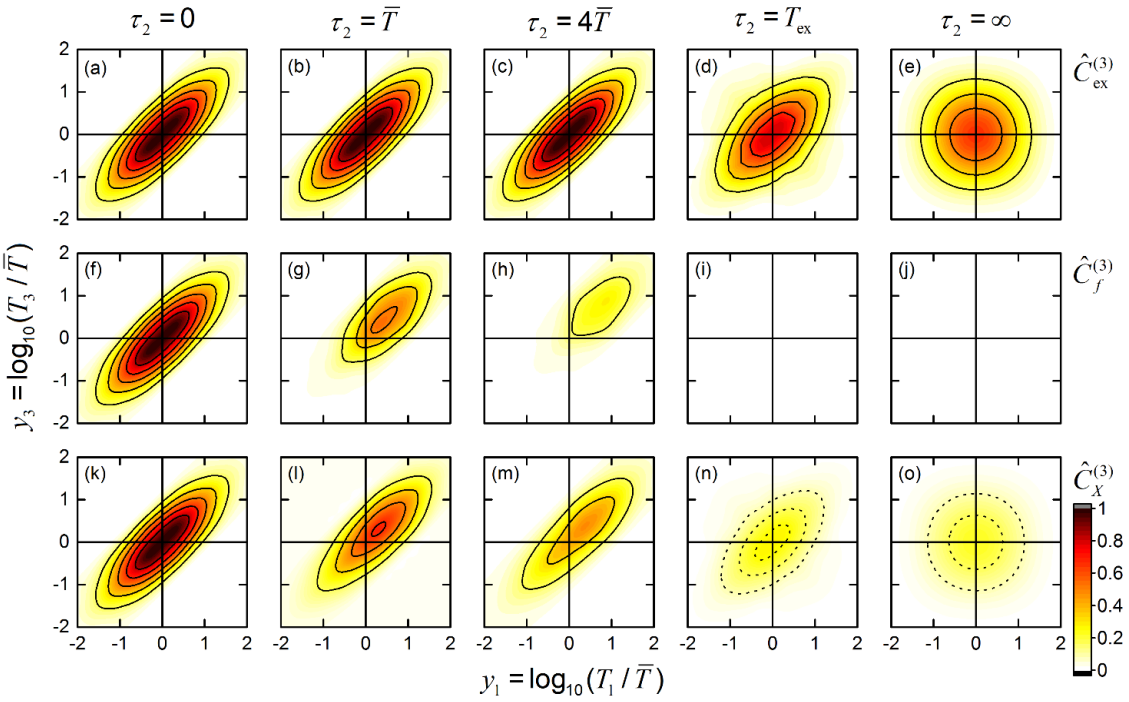

Figure 3.2 Time-dependent rate-correlation spectra for the system of Figure 3.1. Top row: $\hat{C}^{(3)}_{\mathrm{ex}}(y_3,\tau_2,y_1)$, the component that monitors rate exchange. Middle row: $\hat{C}^{(3)}_{f1}(y_3,\tau_2,y_1)$, the component in which the heterogeneity is filtered. Bottom row: The total spectrum $\hat{C}^{(3)}_{X}(y_3,\tau_2,y_1)$. Each row is normalized to a peak of one at $\tau_2 = 0$. The dotted contour interval is half the solid contour interval.

CHAPTER 4

MICELLE HETEROGENEITY FROM THE 2D KINETICS OF SOLUTE ROTATION[2]

[2] Reproduced with permission from Jason R. Darvin and Mark A. Berg *J. Phys. Chem. Lett.* **2019**, *10*, 6885-6899. Copyright 2019 American Chemical Society

4.1 Introduction

In soft, microstructured materials—micelles, vesicles, gels, star polymers, polymer nanoparticles, and so on—there are intertwined questions of where a solute resides and what local properties it sees. The photophysics of a solute that is also a chromophore are often used to gain information.[78-104] Static (0D) measurements, for example, the fluorescence quantum yield or Stokes' shift, give a spatial average of static properties, such as hydrogen-bond availability or polarity. Time-resolved measurements with one time dimension (1D) give rates that characterize dynamic properties. For example, the reorientation or solvation rate characterizes the local viscosity or dielectric-relaxation time, but again, only with an average over locations. In microstructure materials, these 1D kinetics often have nonexponential decays. The implications are clearly important, but the cause is often ambiguous. This chapter shows how 2D kinetics[7,12,25,30,35,61,62,105-109] resolve this problem. MUPPETS (multiple population-period transient spectroscopy)—a 2D version of ultrafast optical spectroscopy;[12,30,35]—is applied to micelles to distinguish between different pictures of the solute distribution and the local properties of a micelle. The rotation time of a dye-molecule solute can be measured by the decay of its optical anisotropy.[110] It is well established that the rotation time reflects the solvent's macroscopic viscosity. In simple solvents, the decay is close to a single exponential, yielding a single viscosity. (Deviations are seen, even in pure solvents, when complexity is added, for example, slow solvation,[111] oligomeric solvents,[11,12,111] or ionic liquids.[112]) When the same experiment is performed in microstructured materials in general, and micelles in particular, the anisotropy decays become nonexponential and appears to have multiple rates.[93-104] (Whether this rate dispersion should be described as a multiexponential (discrete rates) or

as a stretched exponential or other continuous rate distribution is not experimentally decidable, but depends on the model used to describe it. We use a nonparametric approach that does not distinguish between these cases.[108])

A simple explanation for the observed rate dispersion is that it reflects rate heterogeneity.[86,91,92,100] Solute molecules occupy a variety of positions within the micelle, and these positions have different local viscosities. Each solute has a specific microviscosity, a well-defined rotation time, and an exponential anisotropy decay, but 1D kinetics only see the average over the distribution of microviscosities. In this model, the distribution of observed rates can be directly converted into a distribution of viscosities.

A contrasting, but widely accepted,[93-99,101-104] explanation is the "wobble-in-a-cone" model.[113-115] This model is homogeneous. It assumes that every micelle has the average structure, which is strongly layered into a hydrocarbon core, a surface layer of partially hydrated head groups, and the aqueous solvent. It further assumes that the probe is confined to the surface layer, and this layer is strongly anisotropic. As a result, the solute can only "wobble" over a restricted cone of angles about the local director. Other angles are explored more slowly by diffusion to a different point on the surface. In its simplest form, this model predicts a biexponential decay: the fast time gives the viscosity of the surface layer, the slow time gives the layer's diffusion constant, and the relative amplitude is related to the cone angle. Every molecule experiences both fast and slow processes in sequence, and the rates seen on one molecule are also seen on every other molecule. Using 1D kinetics alone, it is difficult, if not impossible, to distinguish between the wobble-in-a-cone and heterogeneity models.

4.2 1D Kinetics of SDS Micelles

The 1D kinetics of pyrromethene 597 (PM597)[116-118] in sodium-dodecyl-sulfate (SDS) micelles119-124 are shown in Figure 4.1. The absorption change with parallel $\Delta A_{\parallel}(\tau)$ and perpendicular $\Delta A_{\perp}(\tau)$ polarizations are converted to the electronic,

$$C_{\mathrm{e}}^{(1)}(\tau) = \frac{\frac{1}{3}\Delta A_{\parallel}(\tau) + \frac{2}{3}\Delta A_{\perp}(\tau)}{\frac{1}{3}\Delta A_{\parallel}(0) + \frac{2}{3}\Delta A_{\perp}(0)} \tag{45}$$

and rotational,

$$C_{\mathrm{r}}^{(1)}(\tau) = \frac{\Delta A_{\parallel}(\tau) - \Delta A_{\perp}(\tau)}{\frac{5}{9}\Delta A_{\parallel}(\tau) + \frac{10}{9}\Delta A_{\perp}(\tau)} \tag{46}$$

decays (Figure 4.1a).[110] [See Appendix A for experimental methods.] The electronic decay is similar to the electronic lifetimes reported for PM597 in other solvents.[116] The rotational decay is also similar to those for other dye molecules in a variety of micelles.[93-104] It is clearly stretched relative to a single exponential. For reference, a stretched-exponential fit ($\exp[(-\tau/T_0)^{\beta}]$, not shown) gives $\beta = 0.66$.

.Because different models imply different fitting functions, we analyze the data with a nonparametric approach, that is, one that does not require a specific form for the fitting function.[108] The data is smoothed (Appendix A) so its derivative can be taken to give the "decay spectrum" (Figure 4.1b),

$$\hat{C}_{\mathrm{r}}^{(1)}(\ln T) = -\left(\frac{\partial C_{\mathrm{r}}^{(1)}(\tau)}{\partial \ln \tau}\right)_{T=\tau} \tag{47}$$

The first moment of this spectrum gives the geometric-mean rotation time, $\bar{T}_r$ = 230 ps. The second central moment (variance) is the total rate dispersion d_{rot} = 3.22, substantially higher than for a single exponential decay (d_{exp} = 1.645).

This decay spectrum contrasts with the more common rate spectrum $\tilde{C}_r^{(1)}(\ln T)$,

$$C_r^{(1)}(\tau) = \int_{-\infty}^{\infty} \tilde{C}_r^{(1)}(\ln T) e^{-\tau/T} d(\ln T) \tag{48}$$

which is an inverse-Laplace transform on a log scale. It expresses the rotational decay as a superposition of exponential decays with time constants T. The advantage of the decay spectrum is that it can be derived uniquely from the data, whereas finding the rate spectrum is well-known to be an ill-posed problem without a unique solution.[125] The precise relationship between the decay and rate spectra is

$$\hat{C}^{(1)} = \tilde{C}^{(1)} * \hat{C}_{exp}^{(1)} \tag{49}$$

where the star indicates convolution on the ln-T scale. Thus, the measurement of the rate spectrum is obscured by a "response function" $\hat{C}_{exp}^{(1)}(\ln T)$, which is the decay spectrum of an exponential decay (green curve in Figure 4.1b). It is a precisely known function, but it obscures the details of the rate spectrum nonetheless. Equation 49 shows that the lack of uniqueness in the rate spectrum is the same as the ambiguity in deconvolution. Because variances add under convolution, we can quantify the degree of stretching by the excess rate dispersion d_{exc}, the difference between the variance of the experimental spectrum d_{rot} and the variance of the response function d_{exp}, $d_{exc} = d_{rot} - d_{exp}$ = 1.58. Broad features, such

as these variances, can be recovered despite the convolution, even though fine features cannot.

A general way to model the dispersion in the rotational decay is to start with a homogenous decay shape $C_{\text{hom}}^{(1)}(\tau / T)$, which is shared by all molecules. For example, it could be the biexponential decay predicted by the wobble-in-a-cone model. It has an excess dispersion d_{hom} or a total dispersion $d_{\text{hom}} + d_{\text{exp}}$. In addition, each molecule may have its own time constant T, which is distributed with a probability $P_{\text{het}}(T)$. Combining this heterogeneous source of rate dispersion with the homogeneous decay give the total decay,

$$C_{\text{rot}}^{(1)}(\tau) = \int_0^\infty C_{\text{hom}}(\tau / T) P_{\text{het}}(T) dT \tag{50}$$

This model assumes that the local time constant does not change during the decay; it is in the slow rate-exchange limit.

With this model,

$$\hat{C}_{\text{r}}^{(1)} = \hat{C}_{\text{hom}} * P_{\text{het}} \tag{51}$$

and

$$d_{\text{rot}} = d_{\text{hom}} + d_{\text{exp}} + d_{\text{het}} \tag{52}$$

where d_{het} is the variance of $P_{\text{het}}(T)$ on a ln-T scale. One-dimensional methods can measure the excess rate dispersion, $d_{\text{exc}} = d_{\text{rot}} - d_{\text{exp}} = d_{\text{hom}} + d_{\text{het}}$, but they provide no means to separate this sum into its components.

4.3 2D Kinetics of SDS Micelles

Two-dimensional kinetics[7,12,25,30,35,61,62,105-109] are sensitive to the difference between homogeneous and heterogeneous rate dispersion.[35] In these experiments, there are two excitations of the sample separated by a time interval τ_1. A measurement of the state of the system and its return to equilibrium occurs after a second period τ_2, measured from the second excitation. If the response of the system is nonlinear, this signal differs from the sum of the signals from each excitation individually. This difference is the 2D decay $C^{(2)}(\tau_2, \tau_1)$.

MUPPETS is a version of 2D kinetics based on ultrafast optical excitation of electronic states.[35] Each excitation is a pair of simultaneous laser pulses crossed at the sample to produce a spatial grating of excited states. The final measurement is by heterodyned diffraction from the mixed grating created by the nonlinear interaction of both excitations. This configuration requires a six-pulse sequence, but results in single-shot cancellation of the 1D signals from each excitation acting individually. The optical system used to generate this pulse sequence is described in the Appendix A.

When using polarized pulses, there are four unique correlation functions differing by the type of dynamics measured in each time interval: rotation–rotation, electronic–electronic, symmetric rotation–electronic, and asymmetric rotation–electronic. The first two can be isolated with measurements at only two polarization combinations: $\Delta A_{++}(\tau_2, \tau_1)$ and $\Delta A_{-+}(\tau_2, \tau_1)$ (see Figure A.4a in Appendix A).[12] These can be added to give the electronic–electronic correlation,

$$C_{ee}^{(2)}(\tau_2,\tau_1)=\frac{\frac{7}{12}\Delta A_{++}(\tau_2,\tau_1)+\frac{5}{12}\Delta A_{+-}(\tau_2,\tau_1)}{\frac{7}{12}\Delta A_{++}(0,0)+\frac{5}{12}\Delta A_{+-}(0,0)} \tag{53}$$

or subtracted to give the rotation–rotation correlation,

$$C_{rr}^{(2)}(\tau_2,\tau_1)=\frac{\Delta A_{++}(\tau_2,\tau_1)-\Delta A_{+-}(\tau_2,\tau_1)}{\frac{7}{12}\Delta A_{++}(\tau_2,\tau_1)+\frac{5}{12}\Delta A_{+-}(\tau_2,\tau_1)} \tag{54}$$

The resulting electronic–electronic surface is shown in Figure 4.2a as a set of slices at fixed τ_1. The 1D decay (Figure 4.1a) is nearly single exponential. There is an additional small component that is attributed to electronic-state solvation, which causes a spectral shift and a slight drop in cross section at early times. Thus, no heterogeneity is expected. The solid curves are predicted from the 1D electronic decay, making this assumption. The data in Figure 4.2a do not deviate from the predictions in a systematic way as τ_1 increases. This result indicates that there is no heterogeneity in the electronic-state relaxation. Attention can focus on the more interesting rotational dynamics.

The rotation–rotation results are shown in Figure 4.2b. Careful examination shows that these shapes do change systematically as τ_1 increases; small τ_1 curves begin decaying earlier than curves with a large τ_1. This result indicates that rate heterogeneity is important in the rotational dynamics. For a more quantitative interpretation, the data are smoothed and converted to a 2D decay spectrum (Appendix A). The smoothing surface is shown as the curves in Figure 4.2b; the corresponding spectrum is shown in Figure 4.3b.

A 2D decay spectrum indicates the degree of correlation between the time constant T_1 that a molecule has during τ_1 and the time constant T_2 that it has during τ_2. For heterogeneous rate dispersion, each time constant has a distribution throughout the sample;

for a specific molecule, there is only one time constant, which is the same in both time intervals. If we could measure the 2D rate spectrum, it would be spread along the diagonal with all the rates of the 1D spectrum, but it would be a delta function along the antidiagonal. However, we can only directly measure the 2D decay spectrum, which is a convolution of the rate spectrum with the spectrum of an exponential (similar to equation 49). Figure 4.3a shows the decay spectrum calculated from the 1D data, assuming only heterogeneous rate dispersion and including this convolution. Despite the convolution, the elongation along the diagonal is clear.

On the other hand, if the rate dispersion is homogeneous, the various rates seen in the 1D data represent sequential steps in a relaxation process that is experienced by every molecule. Even a single molecule will experience all time constants during two separate relaxation events, one during τ_1 and one during τ_2. In a 2D rate spectrum, there would be off-diagonal "cross peaks" at every combination of time constants. Figure 4.3c shows the decay spectrum calculated from the 1D data, assuming only homogeneous rate dispersion and including the convolution with the response function. The spectrum is compact with similar widths along the diagonal and the antidiagonal.

The measured 2D decay spectrum (Figure 4.3b) is strongly elongated, indicating that rate heterogeneity is the primary source of rate dispersion. The same qualitative conclusion can be taken from the time-domain data (Figure 4.2b), but the 2D spectrum makes it more visually evident.

The 2D spectrum is also easy to quantify. In principle, both local anisotropy and local viscosity variation, that is both homogeneous and heterogeneous mechanisms, may be acting simultaneously. Thus, the quantitative question is what fraction of the rate

dispersion is due to rate heterogeneity. Within the slow rate-exchange model (Equation 50) the 2D spectrum can be further reduced to two, 1D projections.[108] The integrations involved result in additional averaging of the experimental noise.

If the 2D spectrum is projected along the vertical (or horizontal) axis, it should give the 1D spectrum. This projection from the 2D spectrum (Figure 4.3b) is compared to the result from the 1D data in Figure 4.1b. They are in good agreement. (The vertical projections of the heterogeneous and homogeneous models in Figures 4.3a and 4.3c agree perfectly with the 1D data, by construction.)

The new information in the 2D spectrum comes from the other projection, which is taken along the diagonal (Figure 4.3d). It has a variance of $d_{\mathrm{dia}} = d_{\mathrm{hom}} + d_{\mathrm{exp}}$; the heterogeneous contribution in equation 52 is absent.[108] For comparison, the projections of the homogeneous and heterogeneous models (Figures 4.3a and 4.3c) are also shown. The data are close to the heterogeneous limit, but there is a slight broadening due to some degree of homogeneous rate dispersion. The effect is small, but eliminating it results in a clear increase in the chi-squared of the fit to the time-domain data (Appendix A).

The variances of these two projections can be combined to give the fraction of the excess rate dispersion that is due to rate heterogeneity,

$$f_{\mathrm{het}} = \frac{d_{\mathrm{het}}}{d_{\mathrm{hom}} + d_{\mathrm{het}}} = \frac{d_{\mathrm{rot}} - d_{\mathrm{dia}}}{d_{\mathrm{rot}} - d_{\mathrm{exp}}} = 87\% \tag{55}$$

When the projections are reduced to their two variances, there is even more averaging of experimental noise. This single number is a reduction or "averaging" of all the data in Figure 4.2. Thus, it is more reliable than one might anticipate. It also does not rely on assumptions about the specific mechanism responsible for either the homogeneous

or heterogeneous rate dispersion or using specific functions to represent $C_{hom}(\tau/T)$ or $P_{het}(T)$. It only assumes the general form of equation 50.

4.4 Viscosity Inside Micelles

Although the 1D data cannot be uniquely decomposed into homogenous and heterogeneous contributions, the loss of information in equation 50 is not complete. The loss primarily affects the high moments of $C_{hom}(\tau/T)$ or $P_{het}(T)$. An example of a decomposition with the correct low moments can be created using the 2D results and mild assumptions. We assign a biexponential to $C_{hom}(\tau/T)$ and a beta distribution to $P_{het}(T)$. The biexponential is the simplest form from the wobble-in-a-cone model for local anisotropy. The beta distribution is a smooth, single peaked function with four adjustable parameters.[126] With these forms, the Appendix A shows that the first four moments of the 1D decay spectrum and the value of f_{het} from the 2D measurements can be correctly reproduced. The resulting inversion of equation 50 correctly represents the major features of $C_{hom}(\tau/T)$ and $P_{het}(T)$, even though the details are not unique.

Figure 4.3d compares $C_{hom}(\tau/T)$ to a single exponential. This comparison correctly illustrates the magnitude of the homogeneous rate dispersion, which in turn, reflects the amount of anisotropy in the solute's local environment. It is quite small, near the limits of experimental detectability.

Figure 4.4 shows the distribution of microviscosities implied by the measurements. The rotation time of PM597 in several pure solvents was measured to establish the relationship between rotation time and viscosity (Appendix A). This figure must be interpreted with the understanding that finer features may be distorted in the deconvolution.

For example, the low viscosity tail may decay too slowly or the high viscosity cut-off may be too sharp. However, the mean position, width and skewness of the distribution are well represented. Thus, microviscosities are significantly populated from levels near, or even below, those of the external water (1 cP) to ones ~30-fold higher. The high viscosity is not simply characteristic of long hydrocarbon chains: the viscosity of dodecane is only 1.3 cP. Rather it is caused by constraints on the motion imposed by the micelle structure. A similarly high viscosity is found in dodecanol (16.1 cP), where motion is constrained by the need to maintain hydrogen bonding between the sparse hydroxyl groups. The skew is strong, with the peak probability near the maximum microviscosity and a steadily decreasing probability for lower microviscosities. This shape has implications for a structural interpretation.

4.5 Conclusions

Many discussions of micelles are based on their average structure. This structure can be seen in measurements that average over many molecules, such as light,[123] x-ray[121] or neutron[120,122] scattering. In a sense, they are mean-field discussions. The wobble-in-a-cone model adds the idea that a solute is tightly confined to a single portion of this structure, resulting in homogenous behavior.

To create the observed heterogeneity, we could keep the mean-field picture of the micelle, but add a strong radial gradient in microviscosity and assume that take the solutes distribute throughout the micelle. However, the highest viscosity would be in the center, which occupies a small volume. The intermediate region has a larger volume and, as a result, most solutes would be in a region of intermediate microviscosity. The strong skew in Figure 4.4 is hard to explain.

On the other hand, we can drop the mean-field picture. Micelles are held together by weak forces, allowing large fluctuations in their instantaneous structure. Heterogeneity arises not just from the variety of conditions within one micelle, but also from the diversity of structures from micelle to micelle. Most structures have a substantial region from which water is excluded and where the solute is most soluble. The need to exclude water constrains motion, creating a high viscosity. In the interfacial region, the water, head groups, and hydrocarbon mix in ways that are much more diverse, with more water exposure leading to sites that are more mobile, but also less favorable to the solute. This picture can account for the broad and highly skewed distribution of microviscosities, if the range of instantaneous configurations persist over the nanosecond duration of the measurement.

The same issues are relevant to other microstructured materials and other processes. These materials are all susceptible to large fluctuations in structure that can persist over times longer than important chemical events. The average structure seen in many experiments only becomes relevant on longer timescales. Two-dimensional kinetics offer a direct approach to probing the properties of such fluctuation

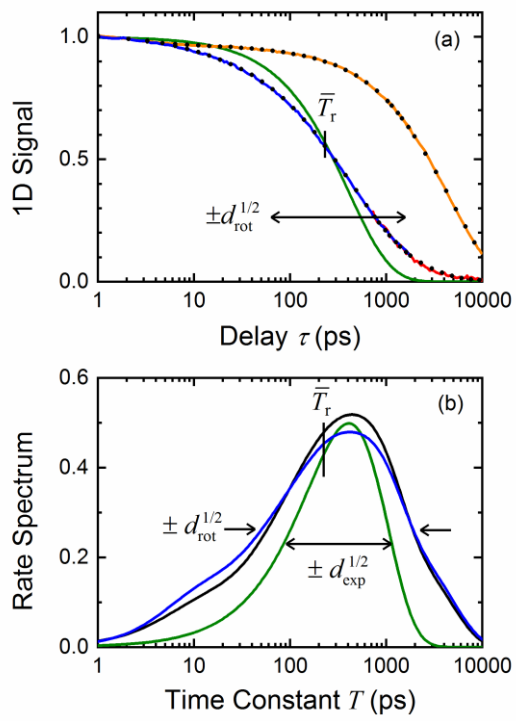

Figure 4.1 The 1D kinetics of PM597 in SDS micelles. (a) The rotational decay $C_r^{(1)}(\tau)$ from pump–probe measurements (blue) and time-correlated single-photon counting (red) is shown as a solid curve. The nonexponential rotational dynamics are characterized by the geometric-mean time $\bar{T}_r$ and the rate dispersion d_{rot}. A single exponential with the same $\bar{T}_r$ (green) and its own dispersion d_{exp} is shown for comparison. A smooth fit (black dots) is used to produce the spectrum in (b). The rotation-free electronic decay $C_e^{(1)}(\tau)$ (orange) is also shown with its smooth fit (black dots). (b) Rotational decay spectra from 1D (black) and 2D (blue) measurements

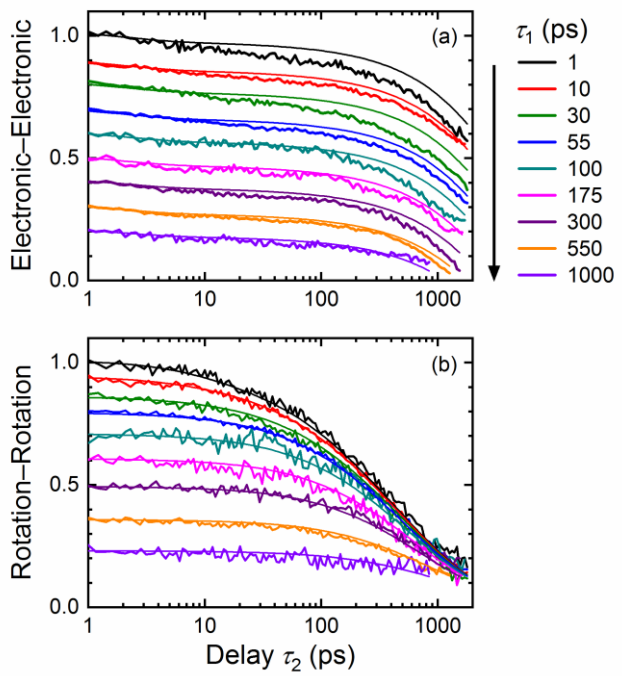

Figure 4.2 The 2D kinetics of PM597 in SDS micelles. The (a) electronic–electronic $C_{ee}^{(2)}(\tau_2,\tau_1)$ and (b) rotation–rotation $C_{rr}^{(2)}(\tau_2,\tau_1)$ surfaces are shown as a series of cuts at constant τ1. The smooth curves in (a) are the predictions from the 1D results, assuming a homogeneous electronic decay. In (b), the curves are a smoothing fit. They are used to produce the decay spectra in Figure 4.3.

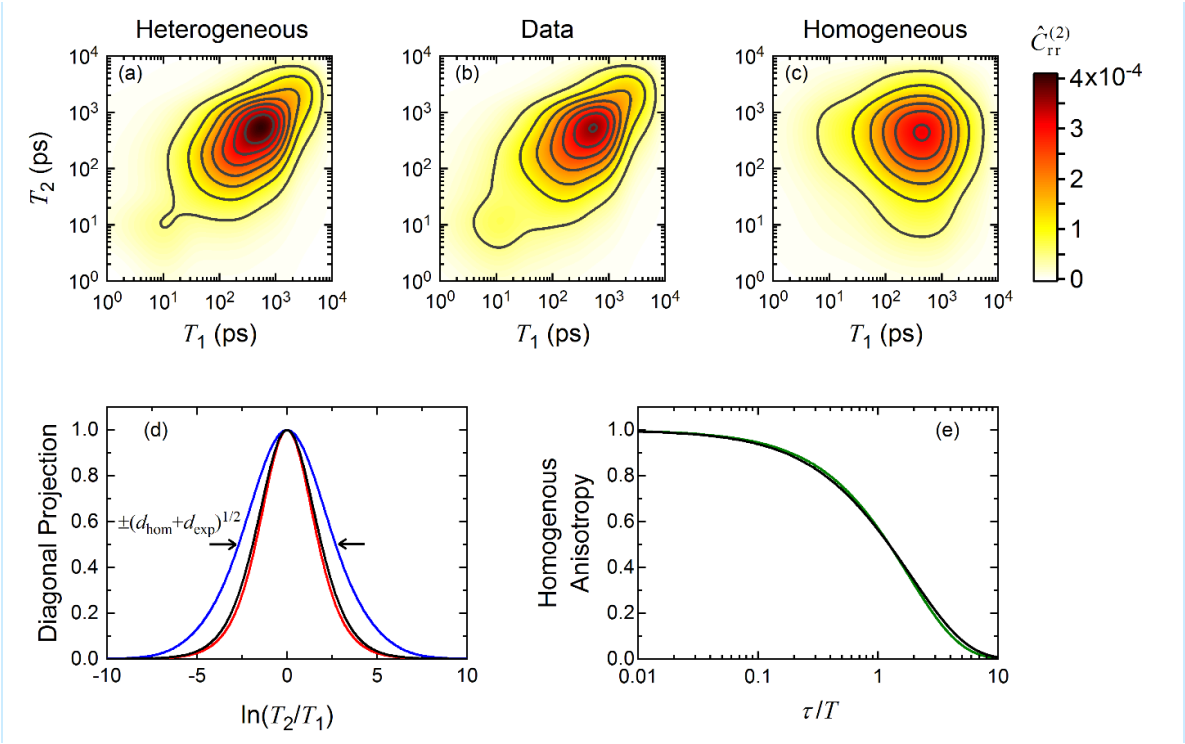

Figure 4.3 Analysis of the rotation–rotation results (Figure 4.2b). The 2D decay spectra $\hat{C}^{(2)}_{rr}(T_2,T_1)$ for (a) 100% heterogeneity and (c) 0% heterogeneity are compared to (b) the measured spectrum. (d) Projections of the decay spectra along the diagonal: 100% heterogeneous (a, red), measured (b, black) and 0% heterogeneous (c, blue). (e) The decay shape for an individual molecule ($C_{hom}(\tau/T)$, black) compared to an exponential (green)

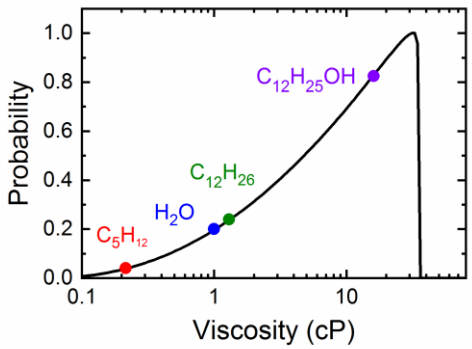

Figure 4.4 The distribution of microviscosities seen by the solute. The viscosities of several pure solvents are marked for reference.

CHAPTER 5

ROTATIONAL ANISOTROPY IN IONIC LIQUIDS

5.1 Introduction

Room temperature ionic liquids, often referred to simply as ionic liquids, are organic salts that exist in the liquid state below 100 °C. There exists many combinations of cation-anion pairs available during the synthesis of ionic liquids allowing for tunable properties. An example of the molecular structure of an ionic liquid is show in figure 5.1. Ionic liquids are of interest to people because almost everything is soluble in them, they possess negligible volatility, and they have a high ionic conductivity. These properties make them ideal for energy, synthesis, or green chemistry applications.[127] Experiments to understand the properties of ionic liquids often exhibit rate dispersion[128-134]; thus, their structural, solvation, and reaction dynamics are poorly understood.

Solvation dynamics study a solvents reorganization around a solute molecule that has undergone a change in its charge distribution. In typical solvents, the solvation response is biphasic caused by inertial motion of the solvent molecules on the femtosecond scale and the diffusion dynamics on the picosecond to nanosecond timescale. It is assumed this dispersion is caused by a homogeneous mechanism.[135] Maroncelli and coworkers[128-134] studied the solvation response of coumarin 153 in ionic liquids and found that the diffusive solvation dynamics are considerably more dispersed than the dynamics seen in common

solvents. In an effort to understand the structural properties of ionic liquids, computer simulations wereby performed Canongia Lopes and Pádua.[136] Their results suggest that ionic liquids are composed of nanostructured nonpolar and polar regions. Nonpolar regions are comprised of the alkyl chains of the cations. Polar regions are comprised of charged portions of the cation and the anion. This study implies structural heterogeneity is responsible for rate dispersion seen in ionic liquids. Terranova and Corcelli.[137] performed molecular dynamics simulations to mimic a solvation response function. The shape of their solvation response function matched experimental results; however, they attribute the shape of the decay to translational movement of the anion in and out of the first solvation shell.

The results of solvation dynamics experiments in ionic liquids bring up an obvious question. Is rate heterogeneity present in the rotational anisotropy of a solute molecule within ionic liquids? This chapter aims to answer that question. The anisotropy of pyrromethene 597 was measured in a series of 1-alkyl-3-methylimidazolium tetrafluoroborate (C_nMIM:BF_4) ionic liquids mixed with acetonitrile at a constant mole fraction and it was measured in 1-dodecyl-3-methylimadazolium tetrafluoroborate (C_{12}MIM:BF_4) at varying mole fraction. In each set of experiments, non-exponential decay was observed, but the magnitude of the dispersion lied within the noise level of the MUPPETS experiment.

5.2 Experimental Details

Ionic liquids were purchased from io-li-tec at ≥ 98% purity. Ionic liquids were stored in a desiccator to eliminate the absorption of water during storage. Pyrromethene 597 (PM597) was purchased from Exciton. Acetonitrile was obtained from Sigma Aldrich

at spectrochemical grade. Ionic liquids and acetonitrile were measured by weight. Mole fractions were relative to the ionic liquid. PM597 was added until the optical density was 0.4. Experiments were performed in a flow cell as a precaution to protect against the formation of photoproducts.

Ultrafast pump probe spectroscopy was used to measure the rotational anisotropy of PM597. The ultrafast optical pulses were approximately 300 fs in length and have a wavelength of 527 nm. Excitation of the sample was performed with pulse 1c at 500 Hz. Measurement of the sample was performed with pulse 3c at 1000 Hz and detected with PD1. A second reference pulse, 3a, did not pass through sample and was detected by PD2. A variable neutral density filter was place in front of PD2 to ensure equal intensity of PD1 and PD2 before the experiment was performed. The signal was calculated by PD1-PD2 with a lock-in amplifier. A fourth pulse, 3b, was placed on PD3 to measure long term fluctuations in laser intensity. The final signal was calculated by (PD1-PD2)/PD3. The vertical polarization of pulse 3c remained constant. The experiment was performed with the polarization of pulse 1c at both vertical and horizontal polarizations (parallel and perpendicular).

5.3 Results and Discussion

The first set of experiments measured the rotational anisotropy of PM597 in a series of ionic liquids at a constant mole fraction. The mole fraction was chosen so that rotation of PM597 in each ionic liquid completely decayed within our two-nanosecond time window. The ionic liquids studied were 1-ethyl-3-methylimidazolium tetrafluoroborate (C_2MIM:BF_4). 1-butyl-3-methylimidazolium tetrafluoroborate (C_4MIM:BF_4), 1-octyl-3-methylimidazolium tetrafluoroborate (C_8MIM:BF_4), and 1-dodecyl-3-methylimidazolium

tetrafluoroborate ($C_{12}MIM:BF_4$) at χ = 0.2. The parallel and perpendicular polarization curves can be seen in figure 5.2.

The tails were manually matched at long times to overlap the electronic decay of PM597. This is necessary to correct for drift in the signal size or laser power. The anisotropy was calculated by equations 45 and 46 and is shown in figure 5.3. Anisotropy curves were fit with a stretched exponential function ($A * \exp(-t/\tau)^{\beta}$) where β = 1 represents a single exponential. Rotation times (τ) ranged from 93.9 ps ($C_2MIM:BF_4$) to 246.2 ps ($C_{12}MIM:BF_4$) and β values approached 0.8 for $C_8MIM:BF_4$ and $C_{12}MIM:BF_4$. Full fit parameters are shown in table 5.1. This indicated the presence of rate dispersion; however, the amount of rate dispersion was less than anticipated. The magnitude of the rate dispersion, assuming a heterogeneous mechanism, lies within the noise level of the MUPPETS experiment. It was not viable for this experiment to move forward.

The second set of experiments measured the rotational anisotropy of PM597 in $C_{12}MIM:BF_4$ at varying mole fraction. Mole fractions of 0.2, 0.4, and 0.6 were measured. The rotational anisotropy of PM597 in pure acetonitrile was also measured. Polarization curves for the $C_{12}MIM:BF_4$ and acetonitrile experiments are shown in figure 5.5. Tail matching was performed for acetonitrile and χ = 0.2. The rotational decay for χ = 0.4 and χ = 0.6 was not complete within our two-nanosecond time window. Tail matching for χ = 0.4 and χ = 0.6 was performed by measuring the rotational anisotropy of PM597 in toluene and making the same tail matching correction to the ionic liquid polarization curves. The sequence of experiments was: 1) $C_{12}MIM:BF_4$ (parallel) 2) toluene (parallel) 3) $C_{12}MIM:BF_4$ (perpendicular) 4) toluene (perpendicular). Anisotropy curves were fit with a stretched exponential function. The anisotropy in acetonitrile was found to be

exponential. The fits to the anisotropy of $\chi = 0.2$, $\chi = 0.4$, and $\chi = 0.6$ had β values of about 0.8. Full fit parameters are shown in table 5.2. The anisotropy in acetonitrile was found to be exponential. The fits to the anisotropy of $\chi = 0.2$, $\chi = 0.4$, and $\chi = 0.6$ had β values of about 0.8. Full fit parameters are shown in table 5.2. Rate dispersion was present at each mole fraction, but there was no increase of rate dispersion as the mole fraction of $C_{12}MIM:BF_4$ increased. As mentioned in the previous paragraph, the magnitude of the rate dispersion lies within the noise level of the MUPPETS experiment.

5.4 Conclusions

Recent work by the Maroncelli group[112] has shown that the rotational anisotropy of solute molecules in $C_4MIM:BF_4$ is significantly non-exponential at low temperatures. When fit to a stretched exponential function, the stretching exponent ranged from $0.4 \leq \beta \geq 0.8$. The β values decreased significantly as the temperature decreased. The anisotropy of 9,10-dimethylacridinium in $C_4MIM:BF_4$ at 292 K had a $\beta = 0.81$ when fit to a stretched exponential. This result is in good agreement with the observations made in this chapter. The cause of rate dispersion in ionic liquids is an unanswered question that is worthy of exploration; however, the experimental conditions necessary to observe significant rate dispersion are not compatible with MUPPETS.

Table 5.1 Fit Parameter for the rotational anisotropy of PM597 in C_nMIM:BF_4

Ionic Liquid	A	τ_{rot}	β
C_2MIM:BF_4	1.00	93.93	0.91
C_4MIM:BF_4	1.00	133.37	0.87
C_8MIM:BF_4	1.00	230.81	0.83
C_{12}MIM:BF_4	1.00	246.17	0.81

Table 5.2 Fit parameters for the rotation anisotropy of PM597 in $C_{12}MIM:BF_4$ at varying mole fraction

$\chi(C_{12}MIM:BF_4)$	A	τ_{rot}	β
0.0	1	34.25	1.00
0.2	1.01	253.76	0.80
0.4	0.98	813.72	0.82
0.6	0.99	1375.87	0.81

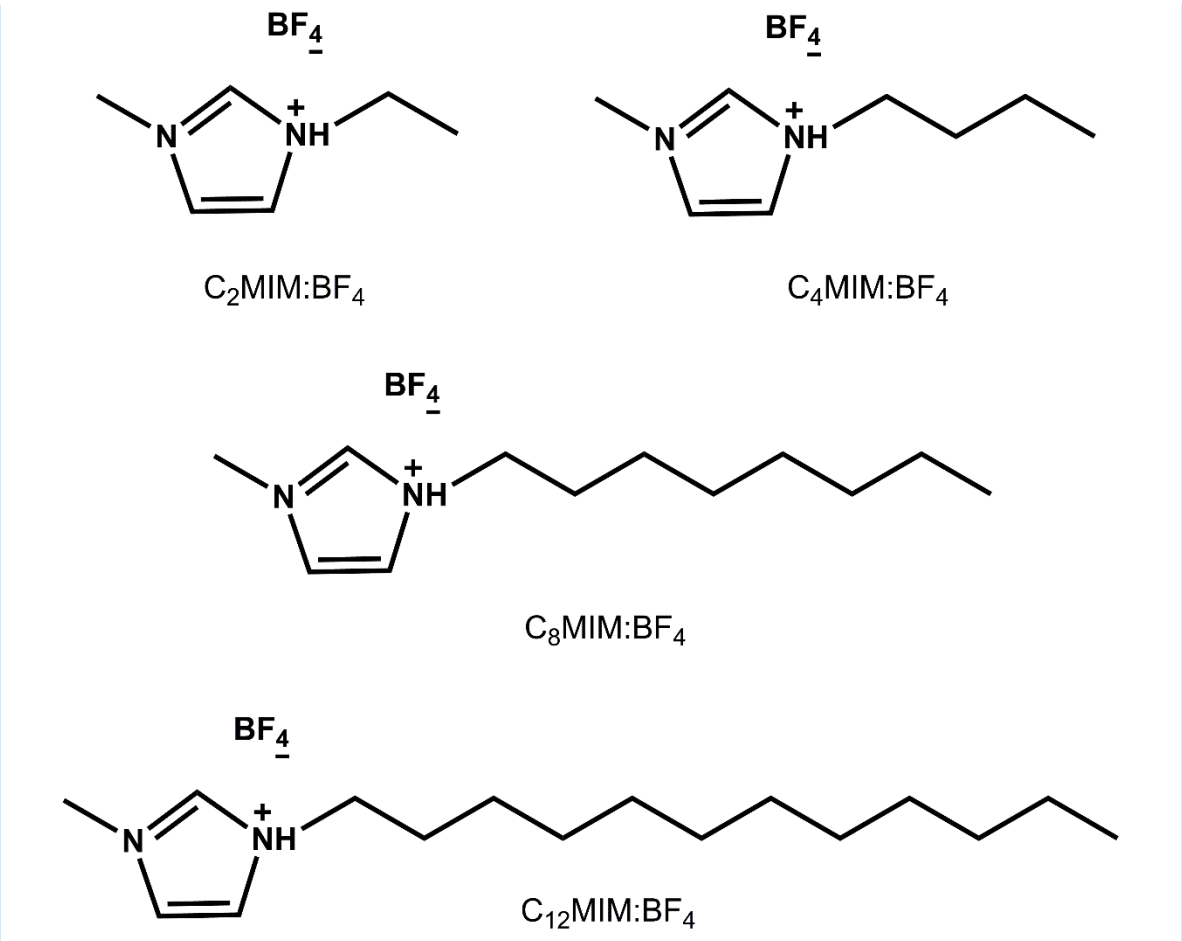

Figure 5.1 The structures of the ionic liquids

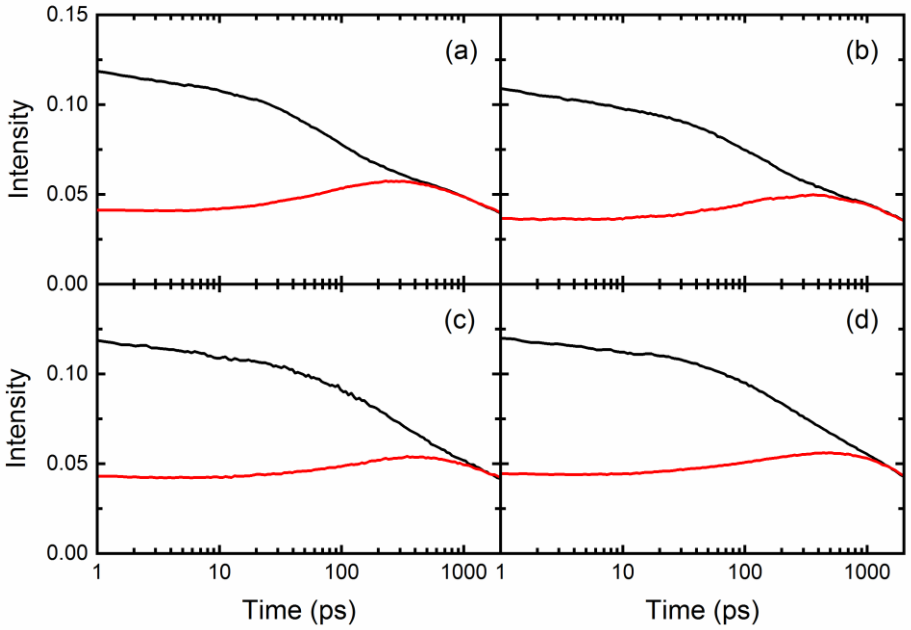

Figure 5.2 Parallel (black) and perpendicular (red) polarization curves for (a) $C_2MIM:BF_4$ (b) $C_4MIM:BF_4$ (c) $C_8MIM:BF_4$ (d) $C_{12}MIM:BF_4$. $\chi = 0.2$ for each ionic liquid.

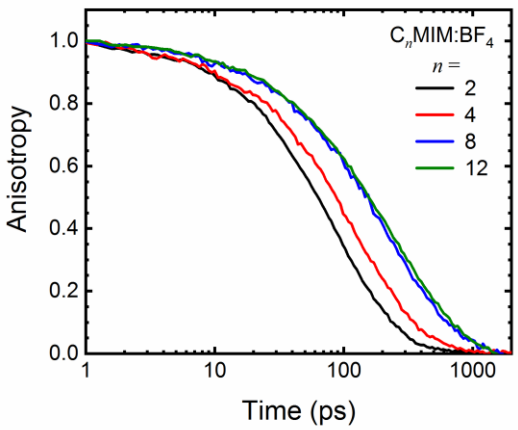

Figure 5.3 Anisotropy curves are shown for $C_2MIM:BF_4$, $C_4MIM:BF_4$, $C_8MIM:BF_4$, and $C_{12}MIM:BF_4$. $\chi = 0.2$ for each ionic liquid

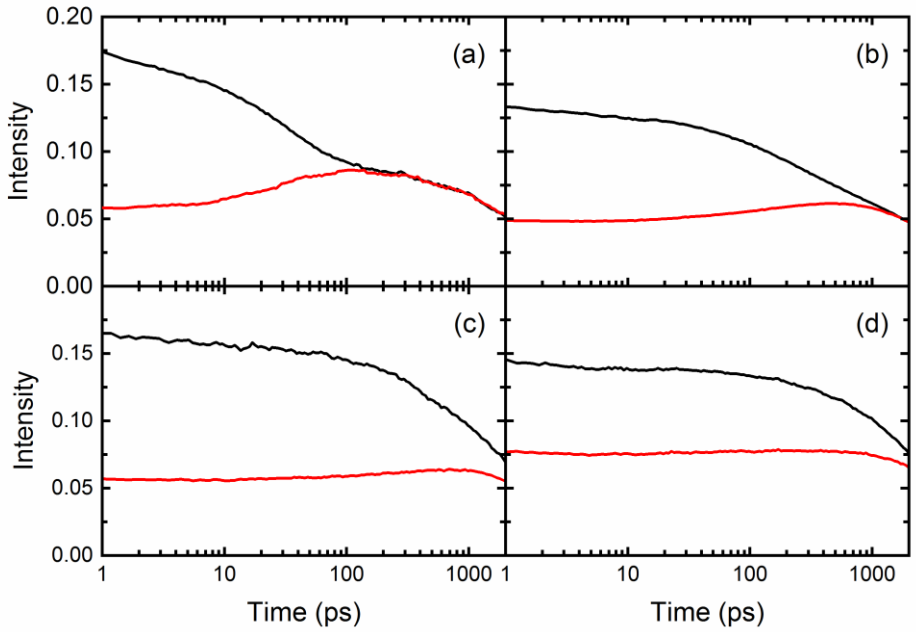

Figure 5.4 Parallel (black) and perpendicular (red) polarization curves for C12MIM:BF4 at (a) $\chi = 0.0$ (pure acetonitrile) (b) $\chi = 0.2$ (c) $\chi = 0.4$ (d) $\chi = 0.6$

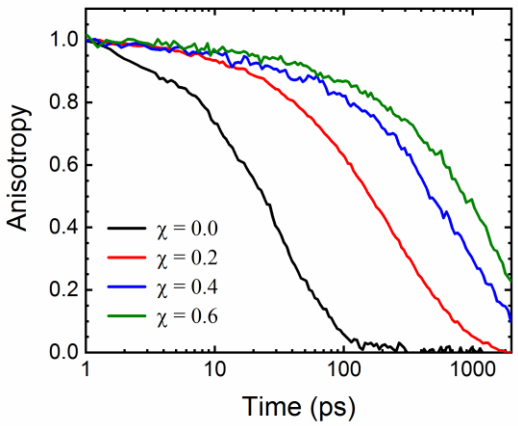

Figure 5.5 Anisotropy curves are shown for $C_{12}MIM:BF_4$ at (a) $\chi = 0.0$ (pure acetonitrile) (b) $\chi = 0.2$ (c) $\chi = 0.4$ (d) $\chi = 0.6$.

REFERENCES

(1) *Disorder Effects on Relaxational Processes: Glasses, Polymers, Proteins*; Richert, R.; Blumen, A., Eds.; Springer: Berlin, 1994.

(2) Ediger, M. D.; Angell, C. A.; Nagel, S. R. *J. Phys. Chem.* **1996**, *100*, 13200.

(3) *Dynamical Heterogeneities in Glasses, Colloids and Granular Media*; Berthier, L.; Biroli, G.; Bouchaud, J.-P.; Cipelletti, L.; van Saarloos, W., Eds.; Oxford University Press: Oxford, 2011.

(4) Kaufman, L. J. *Annu. Rev. Phys. Chem.* **2013**, *64*, 177.

(5) Paeng, K.; Park, H.; Hoang, D. T.; Kaufman, L. J. *Proc. Natl. Acad. Sci. U.S.A.* **2015**, *112*, 4952.

(6) Paeng, K.; Kaufman, L. J. *Macromolecules* **2016**, *49*, 2876.

(7) Verma, S. D.; Vanden Bout, D. A.; Berg, M. A. *Journal of Chemical Physics* **2015**, *143*, 024110.

(8) Ferry, J. D. *Viscoelastic Properties of Polymers*; 3rd ed.; John Wiley & Sons: New York, 1980.

(9) Fuson, M. M.; Hanser, K. H.; Ediger, M. D. *Macromolecules* **1997**, *30*, 5714.

(10) Daniel, S. N.; Niemeyer, E. D.; Bright, F. V. *Macromolecules* **1999**, *32*, 8084.

(11) Somoza, M. M.; Sluch, M. I.; Berg, M. A. *Macromolecules* **2003**, *36*, 2721.

(12) Wu, H.; Berg, M. A. *Journal of Physical Chemistry Letters* **2014**, *5*, 2608.

(13) Xie, X. S. *J. Chem. Phys.* **2002**, *117*, 11024.

(14) Min, W.; Luo, G.; Cherayil, B. J.; Kou, S. C.; Xie, X. S. *Phys. Rev. Lett.* **2005**, *94*, 198302.

(15) Andreatta, D.; Pérez Lustres, J. L.; Kovalenko, S. A.; Ernsting, N. P.; Murphy, C. J.; Coleman, R. S.; Berg, M. A. *J. Am. Chem. Soc.* **2005**, *127*, 7270.

(16) Flomenbom, O.; Velonia, K.; Loos, D.; Masuo, S.; Cotlet, M.; Engelborghs, Y.; Hofkens, J.; Rowan, A. E.; Nolte, R. J. M.; Van der Auweraer, M.; de Schryver, F. C.; Klafter, J. *Proc. Natl. Acad. Sci. U.S.A.* **2005**, *102*, 2368.

(17) Cote, Y.; Senet, P.; Delarue, P.; Maisuradze, G. G.; Scheraga, H. A. *Proc. Natl. Acad. Sci. U.S.A.* **2010**, *107*, 19844.

(18) Yang, S.; Cao, J.; Silbey, Robert J.; Sung, J. *Biophys. J.* **2011**, *101*, 519.

(19) He, W.; Song, H.; Su, Y.; Geng, L.; Ackerson, B. J.; Peng, H. B.; Tong, P. *Nature Commun.* **2016**, *7*.

(20) Samanta, A. *J. Phys. Chem. Lett.* **2010**, *1*, 1557.

(21) Castner, E. W.; Margulis, C. J.; Maroncelli, M.; Wishart, J. F. *Annu. Rev. Phys. Chem.* **2011**, *62*, 85.

(22) Pal, T.; Biswas, R. *J. Chem. Phys.* **2014**, *141*, 104501.

(23) Pal, T.; Biswas, R. *J. Phys. Chem. B* **2015**, *119*, 15683.

(24) Araque, J. C.; Yadav, S. K.; Shadeck, M.; Maroncelli, M.; Margulis, C. J. *J. Phys. Chem. B* **2015**, *119*, 7015.
(25) Verma, S. D.; Corcelli, S. A.; Berg, M. A. *Journal of Physical Chemistry Letters* **2016**, *7*, 504.
(26) Klimov, V. I.; McBranch, D. W.; Leatherdale, C. A.; Bawendi, M. G. *Phys. Rev. B* **1999**, *60*, 13740.
(27) Jones, M.; Lo, S. S.; Scholes, G. D. *Proc. Natl. Acad. Sci. U.S.A.* **2009**, *106*, 3011.
(28) Klimov, V. I. *Annu. Rev. Phys. Chem.* **2007**, *58*, 635.
(29) Kern, S. J.; Sahu, K.; Berg, M. A. *Nano Lett.* **2011**, *11*, 3493.
(30) Sahu, K.; Wu, H.; Berg, M. A. *Journal of the American Chemical Society* **2013**, *135*, 1002.
(31) Kuno, M.; Fromm, D. P.; Hamann, H. F.; Gallagher, A.; Nesbitt, D. J. *J. Chem. Phys.* **2000**, *112*, 3117.
(32) Cichos, F.; von Borczyskowski, C.; Orrit, M. *Curr. Opin. Colloid Interface Sci.* **2007**, *12*, 272.
(33) Wang, M. C.; Uhlenbeck, G. E. *Rev. Mod. Phys.* **1945**, *17*, 323.
(34) Khurmi, C.; Berg, M. A. *J. Chem. Phys.* **2008**, *129*, 064504.
(35) Berg, M. A. *Advances in Chemical Physics* **2012**, *150*, 1.
(36) Cao, J.; Silbey, R. J. *J. Phys. Chem. B* **2008**, *112*, 12867.
(37) Blanco, M.; Walter, N. G. *Methods Enzymol.* **2010**, *472*, 153.
(38) Flomenbom, O. In *Single-Molecule Biophysics: Experiment and Theory*; Komatsuzaki, T., Kawakami, M., Takahashi, S., Yang, H., Silbey, R. J., Eds.; Wiley: Hoboken, New Jersey, 2012; Vol. 146, p 367.
(39) Li, C.-B.; Komatsuzaki, T. *Phys. Rev. Lett.* **2013**, *111*, 058301.
(40) Ochoa, M. A.; Chen, P.; Loring, R. F. *J. Phys. Chem. C* **2013**, *117*, 19074.
(41) Ochoa, M. A.; Zhou, X.; Chen, P.; Loring, R. F. *J. Chem. Phys.* **2011**, *135*, 174509.
(42) Yang, S.; Cao, J. *J. Phys. Chem. B* **2001**, *105*, 6536.
(43) Ronis, D. *Physica A* **1981**, *107*, 25.
(44) van Zon, R.; Schofield, J. *J. Phys. Chem. B* **2005**, *109*, 21425.
(45) van Zon, R.; Schofield, J. *Phys. Rev. E* **2001**, *65*, 011106.
(46) van Zon, R.; Schofield, J. *Phys. Rev. E* **2001**, *65*, 011107.
(47) Barsegov, V.; Mukamel, S. *J. Chem. Phys.* **2002**, *116*, 9802.
(48) Barsegov, V.; Mukamel, S. *J. Chem. Phys.* **2002**, *117*, 9465.
(49) Barsegov, V.; Chernyak, V.; Mukamel, S. *J. Chem. Phys.* **2002**, *116*, 4240.
(50) Kryvohuz, M.; Mukamel, S. *Phys. Rev. A* **2012**, *86*, 043818.
(51) Kryvohuz, M.; Mukamel, S. *J. Chem. Phys.* **2014**, *140*, 034111.
(52) Kryvohuz, M.; Mukamel, S. *J. Chem. Phys.* **2015**, *142*, 212430.
(53) Heuer, A. *Phys. Rev. E* **1997**, *56*, 730.
(54) Heuer, A.; Okun, K. *J. Chem. Phys.* **1997**, *106*, 6176.
(55) Doliwa, B.; Heuer, A. *Phys. Rev. Lett.* **1998**, *80*, 4915.
(56) Flenner, E.; Szamel, G. *Phys. Rev. E* **2004**, *70*, 052501.
(57) Sébastien, L.; Ludovic, B. *J. Phys.: Condens. Matter* **2005**, *17*, S3571.
(58) Kim, K.; Saito, S. *Phys. Rev. E* **2009**, *79*, 060501.
(59) Kim, K.; Saito, S. *J. Chem. Phys.* **2010**, *133*, 044511.

(60) Kim, K.; Saito, S. *J. Non-Cryst. Solids* **2011**, *357*, 371.
(61) Kim, K.; Saito, S. *The Journal of Chemical Physics* **2013**, *138*, 12A506.
(62) Ono, J.; Takada, S.; Saito, S. *The Journal of Chemical Physics* **2015**, *142*, 212404.
(63) Mizuno, H.; Yamamoto, R. *Phys. Rev. E* **2010**, *82*, 030501.
(64) Mizuno, H.; Yamamoto, R. *Phys. Rev. E* **2011**, *84*, 011506.
(65) Mizuno, H.; Yamamoto, R. *J. Chem. Phys.* **2012**, *136*, 084505.
(66) Park, S.-W.; Kim, S.; Jung, Y. *Phys. Chem. Chem. Phys.* **2015**, *17*, 29281.
(67) Senning, E. N.; Lott, G. A.; Fink, M. C.; Marcus, A. H. *J. Phys. Chem. B* **2009**, *113*, 6854.
(68) Mukamel, S. *Principles of Nonlinear Optical Spectroscopy*; Oxford University Press: New York, 1995; Vol. 6.
(69) Berg, M. A. 2016, p unpublished.
(70) Loring, R. F.; Mukamel, S. *Chem. Phys. Lett.* **1985**, *114*, 426.
(71) Stuart, A.; Ord, J. K. *Kendall's Advanced Theory of Statistics*; Oxford University Press: New York, 1987; Vol. 1.
(72) Wu, H.; Berg, M. A. *J. Chem. Phys.* **2013**, *138*, 034201.
(73) *Ultrafast Infrared and Raman Spectroscopy*; Fayer, M. D., Ed.; Marcel Dekker: New York, NY, 2001.
(74) Jonas, D. M. *Annu. Rev. Phys. Chem.* **2003**, *54*, 425.
(75) Kubo, R. *Rep. Prog. Phys.* **1966**, *29*, 255.
(76) Berg, M. A. *J. Chem. Phys.* **2010**, *132*, 144106.
(77) Berg, M. A. *J. Chem. Phys.* **2010**, *132*, 144105.
(78) Vyšniauskas, A.; Kuimova, M. K. *International Reviews in Physical Chemistry* **2018**, *37*, 259.
(79) Demchenko, A. P.; Mély, Y.; Duportail, G.; Klymchenko, A. S. *Biophysical Journal* **2009**, *96*, 3461.
(80) Levinger, N. E. *Current Opinion in Colloid & Interface Science* **2000**, *5*, 118.
(81) Ober, K.; Volz-Rakebrand, P.; Stellmacher, J.; Brodwolf, R.; Licha, K.; Haag, R.; Alexiev, U. *Langmuir* **2019**, *35*, 11422.
(82) Wang, S.; Thorn, A.; Redmond, G. *The Journal of Physical Chemistry C* **2018**, *122*, 6900.
(83) Ahmed, S. A.; Gautam, R. K.; Sharma, P.; Seth, D. *Journal of Photochemistry and Photobiology A: Chemistry* **2018**, *351*, 170.
(84) Samanta, P.; Rane, S.; Bahadur, P.; Dutta Choudhury, S.; Pal, H. *The Journal of Physical Chemistry B* **2018**, *122*, 6079.
(85) Mukherjee, P.; Das, A.; Sen, P. *Journal of Photochemistry and Photobiology A: Chemistry* **2017**, *348*, 287.
(86) Neda, D.; Christina, M. O. *Physical Biology* **2016**, *13*, 066004.
(87) Brandt, E. G.; Edholm, O. *The Journal of Chemical Physics* **2010**, *133*, 115101.
(88) Nojima, Y.; Iwata, K. *The Journal of Physical Chemistry B* **2014**, *118*, 8631.
(89) Das, R.; Duportail, G.; Richert, L.; Klymchenko, A.; Mély, Y. *Langmuir* **2012**, *28*, 7147.

(90) Bhattacharyya, S.; Paramanik, B.; Patra, A. *The Journal of Physical Chemistry C* **2011**, *115*, 20832.
(91) Steege, K. E.; Wang, J.; Uhrich, K. E.; Castner, E. W. *Macromolecules* **2007**, *40*, 3739.
(92) Parasassi, T.; Conti, F.; Glaser, M.; Gratton, E. *Journal of Biological Chemistry* **1984**, *259*, 14011.
(93) Visser, A. J. W. G.; Vos, K.; Van Hoek, A.; Santema, J. S. *Journal of Physical Chemistry* **1988**, *92*, 759.
(94) Quitevis, E. L.; Marcus, A. H.; Fayer, M. D. *Journal of Physical Chemistry* **1993**, *97*, 5762.
(95) Heitz, M. P.; Bright, F. V. *Applied Spectroscopy* **1995**, *49*, 20.
(96) Maiti, N. C.; Krishna, M. M. G.; Britto, P. J.; Periasamy, N. *J. Phys. Chem. B* **1997**, *101*, 11051.
(97) Shirota, H.; Tamoto, Y.; Segawa, H. *Journal of Physical Chemistry A* **2004**, *108*, 3244.
(98) Dutt, G. B. *Langmuir* **2005**, *21*, 10391.
(99) Chakrabarty, D.; Chakraborty, A.; Seth, D.; Hazra, P.; Sarkar, N. *Journal of Chemical Physics* **2005**, *122*, 184516.
(100) Grant, C. D.; Steege, K. E.; Bunagan, M. R.; Castner, E. W. *Journal of Physical Chemistry B* **2005**, *109*, 22273.
(101) Kumbhakar, M.; Mukherjee, T.; Pal, H. *Chemical Physics Letters* **2005**, *413*, 142.
(102) Shiraishi, Y.; Inoue, T.; Hirai, T. *Langmuir* **2010**, *26*, 17505.
(103) Anand, U.; Mukherjee, S. *Langmuir* **2014**, *30*, 1012.
(104) Sonu; Kumari, S.; Saha, S. K. *Physical Chemistry Chemical Physics* **2016**, *18*, 1551.
(105) Guo, Z.; Giokas, P. G.; Cheshire, T. P.; Williams, O. F.; Dirkes, D. J.; You, W.; Moran, A. M. *The Journal of Chemical Physics* **2016**, *145*, 101101.
(106) Phelps, C.; Israels, B.; Marsh, M. C.; von Hippel, P. H.; Marcus, A. H. *The Journal of Physical Chemistry B* **2016**, *120*, 13003.
(107) Kaur, H.; Verma, S. D.; Paeng, K.; Kaufman, L. J.; Berg, M. A. *Physical Review E* **2018**, *98*, 040603(R).
(108) Berg, M. A.; Kaur, H. *Journal of Chemical Physics* **2017**, *146*, 054104.
(109) Berg, M. A.; Darvin, J. R. *Journal of Chemical Physics* **2016**, *145*, 054119.
(110) Fleming, G. R. *Chemical Applications of Ultrafast Spectroscopy*; Oxford University Press: Oxford, 1986.
(111) Horng, M. L.; Gardecki, J. A.; Maroncelli, M. *The Journal of Physical Chemistry A* **1997**, *101*, 1030.
(112) Rumble, C. A.; Uitvlugt, C.; Conway, B.; Maroncelli, M. *The Journal of Physical Chemistry B* **2017**, *121*, 5094.
(113) Kinosita, K.; Kawato, S.; Ikegami, A. *Biophysical Journal* **1977**, *20*, 289.
(114) Halle, B.; Wennerström, H. *The Journal of Chemical Physics* **1981**, *75*, 1928.
(115) Szabo, A. *The Journal of Chemical Physics* **1984**, *81*, 150.
(116) Bañuelos Prieto, J.; López Arbeloa, F.; Martínez Martínez, V.; Arbeloa López, T.; López Arbeloa, I. *Journal of Physical Chemistry A* **2004**, *108*, 5503.

(117) Montejano, H. A.; Amat-Guerri, F.; Costela, A.; García-Moreno, I.; Liras, M.; Sastre, R. *Journal of Photochemistry and Photobiology A: Chemistry* **2006**, *181*, 142.

(118) Costela, A.; García-Moreno, I.; Pintado-Sierra, M.; Amat-Guerri, F.; Sastre, R.; Liras, M.; Arbeloa, F. L.; Prieto, J. B.; Arbeloa, I. L. *Journal of Physical Chemistry A* **2009**, *113*, 8118.

(119) Quina, F. H.; Nassar, P. M.; Bonilha, J. B. S.; Bales, B. L. *The Journal of Physical Chemistry* **1995**, *99*, 17028.

(120) Bergström, M.; Skov Pedersen, J. *Physical Chemistry Chemical Physics* **1999**, *1*, 4437.

(121) Hammouda, B. *Journal of Research of the National Institute of Standards and Technology* **2013**, *118*, 151.

(122) Gubaidullin, A. T.; Litvinov, I. A.; Samigullina, A. I.; Zueva, O. S.; Rukhlov, V. S.; Idiyatullin, B. Z.; Zuev, Y. F. *Russian Chemical Bulletin* **2016**, *65*, 158.

(123) Missel, P. J.; Mazer, N. A.; Benedek, G. B.; Carey, M. C. *J. Phys. Chem.* **1983**, *87*, 1264.

(124) Bezzobotnov, V. Y.; Borbely, S.; Cser, L.; Farago, B.; Gladkih, I. A.; Ostanevich, Y. M.; Vass, S. *The Journal of Physical Chemistry* **1988**, *92*, 5738.

(125) Istratov, A. A.; Vyvenko, O. F. *Review of Scientific Instruments* **1999**, *70*, 1233.

(126) Johnson, N. L.; Kotz, S.; Balakrishnan, N. *Continuous Univariate Distributions*; John Wiley & Sons: New York, 1995; Vol. 2.

(127) Armand, M.; Endres, F.; MacFarlane, D. R.; Ohno, H.; Scrosati, B. *Nat Mater* **2009**, *8*, 621.

(128) Arzhantsev, S.; Ito, N.; Heitz, M.; Maroncelli, M. *Chemical Physics Letters* **2003**, *381*, 278.

(129) Arzhantsev, S.; Jin, H.; Baker, G. A.; Maroncelli, M. *The Journal of Physical Chemistry B* **2007**, *111*, 4978.

(130) Jin, H.; Li, X.; Maroncelli, M. *The Journal of Physical Chemistry B* **2007**, *111*, 13473.

(131) Maroncelli, M.; Zhang, X.-X.; Liang, M.; Roy, D.; Ernsting, N. P. *Faraday Discussions* **2012**, *154*, 409.

(132) Zhang, X. X.; Liang, M.; Ernsting, N. P.; Maroncelli, M. *The journal of physical chemistry. B* **2013**, *117*, 4291.

(133) Zhang, X. X.; Liang, M.; Hunger, J.; Buchner, R.; Maroncelli, M. *The journal of physical chemistry. B* **2013**, *117*, 15356.

(134) Liang, M.; Zhang, X. X.; Kaintz, A.; Ernsting, N. P.; Maroncelli, M. *The journal of physical chemistry. B* **2014**, *118*, 1340.

(135) Gardecki, J.; Horng, M. L.; Papazyan, A.; Maroncelli, M. *Journal of Molecular Liquids* **1995**, *65–66*, 49.

(136) Canongia Lopes, J. N. A.; Padua, A. A. H. *J. Phys. Chem. B* **2006**, *110*, 6.

(137) Terranova, Z. L.; Corcelli, S. A. *The journal of physical chemistry. B* **2013**, *117*, 15659.

APPENDIX A

SUPPLEMENTAL INFORMATION FOR CHAPTER 4

A1 Experimental Methods

A1.1 Sample

The sample consisted of an aqueous solution of sodium dodecyl sulfate (SDS, 200 mM) and pyrromethene 597 (PM597, 52 μM) in a 1.0 mm flow cell at 22 °C (see Figure A.1). The solution had an optical density of 0.39 at the excitation wavelength of 530 nm. At this concentration, the SDS forms micelles containing ~80 molecules.[119-124] The micelles are crowded enough to have correlations in the inter-micelle positions, but they are not crowded enough to perturb the internal structure of the micelles. To confirm this conclusion, 1D measurements at SDS concentrations of 150 mM and 100 mM with the same dye concentration were made, but showed no difference from the 200 mM sample.

PM597 has simple photochemistry: high quantum yield, low triplet yield, weak excited-state absorption, good photostability and weak solvatochromism.[116-118] The sample had an average of one PM597 molecule per 46 micelles, so dye interactions are not expected. To confirm this expectation, the dye concentration was varied to give sample optical densities between 0.17–0.64. No effect on the 1D measurements was found. PM597 is poorly soluble in water: a saturated solution has an optical density of 8×10^{-4} in 1.0 mm. The signal from PM597 independent of a micelle can be neglected.

A1.2 Optical System

The laser pulses were generated by a standard, 1-kHz Ti:sapphire laser system. The signal from a white-light-seeded optical parametric generator was mixed with 800 nm pulses to generate pulses at 530 nm with a bandwidth of 150 cm^{-1}. At the sample, the pulses had a length of ~300 fs (not bandwidth limited) and an energy of 80 nJ/pulse.

The MUPPETS current optical system is shown in Figure A.2. Its design and operation have been described in detail elsewhere.[12,35] The initial pulse is split equally in the vertical direction into first excitation (1), second excitation (2), and probe (3) by a transmission grating (G1). Waveplates (WP) and polarizer P2 were used to adjust the polarizations at the sample to the required combinations (Figure A4a). Extinction ratios were in the range 500–5000 at the sample. A second grating (G2) further divided the pulses into nine equal intensity pulses (Figure A.2, left cross-section). Three pulses were blocked to leave the six pulses used for the experiment (Figure A.2, right cross-section). The differential heterodyne detection required unequal probe intensities at the sample.[A1] One of the phase plates was also a neutral density filter (ND, optical density 1.0, pulse 3c). A compensating variable neutral density (VND) filter was placed in beam 3a.

In polarization measurements, it is common to make a "G-factor" correction by matching the tails of the signals at long times, when rotation is complete. Because those times lie outside our 2-ns time window, we made several changes to the MUPPETS set-up to improve its stability across multiple scans: (1) Fine angle adjustments were added to lens L5 to correct for residual coma. (2) A magnifying doublet lens and camera (not shown) were used to image the beams at the sample position. This system can detect self-focusing, spherical aberration, horizontal and vertical coma, and horizontal and vertical

astigmatism. Each of these problems can be systematically corrected by appropriate adjustments of the main (L4, L5) and meniscus (ML1, ML2) lenses. (3) A slow response (300 ms) photodiode (PD3) independently measured fluctuations in the laser power, which were used to correct both 1D and 2D measurements. (4) Phase plates (PP) have been added to all the beams to allow phase shifts in the excitations.

It was found that residual signal from low-order processes were a significant cause of long term drift and instability, so additional measures were taken to remove them by fast modulation. The first excitation and probe were amplitude modulated by two choppers. The second excitation (2a and 2b) was modulated by chopper C1; pulse 1c was modulated by chopper C2. Both choppers operated at 250 Hz, but with a 90° phase shift, that is, shifted by one pulse period. The signal was detected at 500 Hz with the phase set to give no signal when the pulse 1c was blocked.

A2 1D Measurements

Pump–probe measurements out to 2 ns were made on the same system using pulses 1c and 3c. The raw data are shown in Figure A.3. The time range was extended using measurements by time-correlated single-photon counting (150 ps FWHM instrument response function, 373 nm excitation, 560 nm detection) on a sample with an optical density of 0.10. Anisotropy results for times >700 ps and electronic results for times >1 ns were matched to the pump–probe data in the overlapping regions to create data sets over times from 1 ps – 10 ns. Measurements were taken at parallel $\Delta A\|(\tau)$, perpendicular $\Delta A_{\perp}(\tau)$ and magic-angle $\Delta A_m(\tau)$ polarizations. The amplitudes of the parallel and perpendicular decays were adjusted slightly to match the sum to the magic-angle results before calculating the anisotropy.

A3 2D Measurements

The 2D signal $\Delta A_p(\tau_2, \tau_1; \varphi)$ is a change in absorbance as a function of two time separations, τ_1 and τ_2, phase φ and polarization conditions p. This signal was recorded as sets of scans along τ_2 at a fixed value of τ_1. Scans were taken at each of the four polarization combinations shown in Figure A4a. The (++/−−) and (+−/−+) pairs should be identical. All four polarizations were measured to check for consistency and to improve averaging. The phase of the second excitation (beam 2b) was adjusted for either maximum positive (0°) or maximum negative (180°) signal. Measurements at other phases at τ_1 = 1 ps showed a constant phase, so only these two phases were needed. All polarizations were measured at both phases, giving a total of eight scans in a set (Figure A4b). These scans were combined to give

$$\begin{aligned}\Delta A_{++}(\tau_2,\tau_1) = \Delta A_{++}(\tau_2,\tau_1;0°) - \Delta A_{++}(\tau_2,\tau_1;180°) \\ +\Delta A_{--}(\tau_2,\tau_1;0°) - \Delta A_{--}(\tau_2,\tau_1;180°)\end{aligned} \quad \text{(A56)}$$

and

$$\begin{aligned}\Delta A_{+-}(\tau_2,\tau_1) = \Delta A_{+-}(\tau_2,\tau_1;0°) - \Delta A_{+-}(\tau_2,\tau_1;180°) \\ +\Delta A_{-+}(\tau_2,\tau_1;0°) - \Delta A_{-+}(\tau_2,\tau_1;180°),\end{aligned} \quad \text{(A57)}$$

which are shown in Figure A4c.

Because each set was typically taken on a separate day, their amplitudes and noise levels varied. To correct this variation, a preliminary, multiexponential fit (Equation A60) was made to each fixed-τ_1 curve to extract initial values, $\Delta A_{++}(1ps, \tau_1)$ and $\Delta A_{+-}(1ps, \tau_1)$, and residuals. The chi-squared values of the residuals were used to weight the later fitting. The amplitude of $\Delta A_{++}(\tau_2, \tau_1)$ and $\Delta A_{+-}(\tau_2, \tau_1)$ were individually adjusted to match the τ_1

= 1 ps scan, assuming τ_1–τ_2 symmetry, $\Delta A_p(\tau_2, 1ps) = \Delta A_p(1ps, \tau_1)$. These adjustments effectively combine sequences of 1D slices into unified, 2D surfaces.

The weighted sum of $\Delta A_{++}(\tau_2, \tau_1)$ and $\Delta A_{+-}(\tau_2, \tau_1)$ (Equation 54) formed the electronic–electronic decays shown in Figures A4d and 4.2a. For homogeneous electronic relaxation, the 2D result can be predicted from the 1D results:

$$C_{\mathrm{ee}}^{(2)}(\tau_2, \tau_1) = C_{\mathrm{e}}^{(1)}(\tau_2) C_{\mathrm{e}}^{(1)}(\tau_1) \tag{A58}$$

(solid curves in Figure 4.2a, Table A.2). These results matched the data. Because the 1D results are more accurate, the results of equation A58 were used in equation A62 and to corrected the anisotropy–anisotropy results (equation A59) to the rotation–rotation decay (equation 54).

The difference of $\Delta A_{++}(\tau_2, \tau_1)$ and $\Delta A_{+-}(\tau_2, \tau_1)$ is the 2D anisotropy–anisotropy decay,

$$C_{\mathrm{aa}}^{(2)}(\tau_2, \tau_1) = \frac{\Delta A_{++}(\tau_2, \tau_1) - \Delta A_{+-}(\tau_2, \tau_1)}{\frac{7}{12}\Delta A_{++}(0,0) + \frac{5}{12}\Delta A_{+-}(0,0)}. \tag{A59}$$

An example is shown in Figure A.4d. In the end, the anisotropy–anisotropy decay is divided by the electronic–electronic decay to give the rotation–rotation decay (Equation 54, Figure 4.2b). However, all the intermediate data reduction was done on this anisotropy–anisotropy decay.

A4 Nonparametric Data Reduction

A4.1 1D Spectrum

The 1D anisotropy and electronic decay data were each fit to

$$C_{\mathrm{a/e}}^{(1)}(\tau_1) = \sum_{i=0}^{N} \tilde{c}_{\mathrm{a/e},i}^{(1)} \exp\left(-\tau_1/T_i\right) \tag{A60}$$

with fixed $T_i = 4^i \times 2$ ps. For the anisotropy decay, $N = 5$; for the electronic decay, $N = 7$. The fits are shown in Figure A.3 and the values of $\tilde{c}_{\mathrm{a/e},i}^{(1)}$ are given in Table A.1.

This fit does not have physical significance; it only encodes our expectation that the signal decays smoothly and monotonically. Hundreds of data points containing both signal and noise are reduced to a few coefficients representing the signal. Residuals from the fit represent the noise that is removed when the number of degrees of freedom is reduced. The chi-squared of the fit could be decreased further by decreasing the spacing of the T_i and increasing the number of $\tilde{c}_{\mathrm{a/e},i}^{(1)}$. However, we would start "fitting the noise"; the result would be less smooth and would include more noise.

This fit was used to calculate the 1D rate spectrum (equation 47), and this spectrum is further reduced to the final parameters, $\bar{T}_{\mathrm{r}}$ and d_{rot}. Although equation A60 is a specific functional form, it is chosen only for mathematical convenience, and it is only used as an intermediate representation of the signal. Any other form that goes through the data equally well would give indistinguishable spectra and final parameters.

The set of $\tilde{c}_{\mathrm{a/e},i}^{(1)}$ can be regarded as a rate spectrum of the data. However, rate spectra are never unique and many other spectra would represent the data equally well. For example, the later part of the electronic decay is well fit by a single exponential with a 4.8 ns time constant. The negative coefficients at 512 and 32,768 ps are the result of representing it with exponentials with different, fixed time constants.

A4.2 Initial 2D Spectrum

A similar procedure was applied to the 2D anisotropy, but with the 2D extension of equation A60:

$$C_{\mathrm{aa}}^{(2)}(\tau_2,\tau_1) = \sum_{\substack{j,i=0 \\ j>i}}^{5} \tilde{c}_{\mathrm{aa},ij}^{(2)} \Big[\exp\left(-\tau_2/T_j\right)\exp\left(-\tau_1/T_i\right) + \exp\left(-\tau_2/T_i\right)\exp\left(-\tau_1/T_j\right) \Big] + \sum_{i=0}^{5} \tilde{c}_{\mathrm{aa},ii}^{(2)} \exp\left(-\tau_2/T_i\right)\exp\left(-\tau_1/T_i\right) \quad . \tag{A61}$$

Symmetry in τ_2–τ_1 and in the resulting coefficient matrix is enforced, $\tilde{c}_{\mathrm{a},ij}^{(2)} = \tilde{c}_{\mathrm{a},ji}^{(2)}$, reducing the number of degrees of freedom to 21. Ultimately, the 2D measurement holds only one piece of new information, the degree of heterogeneity. Thus, even reducing the data to 21 degrees of freedom still leaves significant flexibility.

The fit was done with singular-value decomposition, which allows the number of degrees of freedom to be systematically reduced by setting large singular values to zero.[A2] The fitting procedure forces the corresponding linear combinations of the $\tilde{c}_{\mathrm{a},i}^{(1)}$ to zero, creating a smoother spectrum at the expense of a higher chi-squared. Whether the higher chi-squared represents a loss of fidelity to the signal or a greater rejection of noise relies on the judgement of the analyst.

The 2D anisotropy–anisotropy spectrum with eight degrees-of-freedom is shown in Figure A.5. Two features are evident. The main peak is strongly elongated along the diagonal, indicating strong rate heterogeneity. In addition, there are weak cross-peaks near (2 ps, 2 ns). These cross-peaks could be due to leakage of electronic–electronic signal into

the anisotropy–anisotropy measurements. The electronic–electronic spectrum has similar cross-peaks between the fast solvation process and the slow electronic state lifetime. The polarization conditions were calculated for collinear beams, whereas in the experiment, the beams intersect at angles up to 3° from the center line, slightly modifying the correct polarization angles. This systematic error could allow electronic–electronic signal to leak into our anisotropy measurements.

A4.3 Refined 2D Spectrum

These observations led us to a more refined fitting procedure that allows us to include more of our theoretical expectations. We used this function:

$$\begin{aligned} C_{\mathrm{aa}}^{(2)}(\tau_2,\tau_1) = {} & A_{\mathrm{a}} \sum_{i=0}^{5} \tilde{c}_{\mathrm{a},i}^{(1)} \tilde{c}_{\mathrm{a},i}^{(1)} \exp\left(-\tau_2/T_i\right) \exp\left(-\tau_1/T_i\right) \\ & + A_{\mathrm{e}} \sum_{j,i=0}^{7} \tilde{c}_{\mathrm{ee},ij}^{(2)} \left[\exp\left(-\tau_2/T_j\right) \exp\left(-\tau_1/T_i\right) \right] \\ & + \sum_{j=\max(0,i-1)}^{\min(5,i)} \sum_{i=0}^{5} \delta\tilde{c}_{\mathrm{aa},ij}^{(2)} \begin{bmatrix} \exp\left(-\tau_2/T_j\right) \exp\left(-\tau_1/T_i\right) \\ + \exp\left(-\tau_2/T_i\right) \exp\left(-\tau_1/T_j\right) \end{bmatrix} \end{aligned} \tag{A62}$$

The first line represents a fully heterogeneous anisotropy spectrum, as predicted from the 1D data. Using this term incorporates our expectation that the 1D and 2D spectra are consistent with each other. Using this term alone ($A_{\mathrm{e}} = 0$, $\delta\tilde{c}_{\mathrm{e},ij}^{(2)} = 0$), leaves only one degree of freedom in the fit, the amplitude A_{a}. It gives the chi-squared shown by the green square in Figure A.6.

The second term represents leakage of the electronic–electronic signal. The coefficients $\tilde{c}_{\mathrm{ee},ij}^{(2)}$ are already determined, so only the amplitude A_{e} is varied. Adding this

degree of freedom reduces the chi-squared significantly (blue square in Figure A6) with a small A_e.

The third term in equation 62 creates deviations from heterogeneous behavior. The coefficients $\delta\tilde{c}^{(2)}_{aa,ij}$ allow intensity to move from the diagonal regions to off-diagonal ones. Because the central peak is expected to broaden, the transfer was limited to near-diagonal regions of the spectrum, that is, to next-to-diagonal coefficients. Attempts to include coefficient farther from the diagonal did not improve the fit.

The coefficients $\delta\tilde{c}^{(2)}_{aa,ij}$ were fit while the amplitudes A_a and A_e were fixed at their previously determined values. The procedure was then iterated: The fit to A_a and A_e was repeated with fixed $\delta\tilde{c}^{(2)}_{aa,ij}$ (giving a final result, A_e = 4.7%) and then the $\delta\tilde{c}^{(2)}_{aa,ij}$ were refit with fixed A_a and A_e. The reiteration gave only a small change.

The squares in Figure A.6 shows the value of chi-squared with the number of degrees of freedom in the final fit. The spectrum in Figure 4.3b and the remaining analysis were based on the fit with five degrees of freedom. Based purely on measures internal to the data set, chi-squared and number of degrees of freedom, this description of the data is equivalent to the initial spectrum in Figure A.5. However, the refined fit better incorporates external information: it gives a vertical projection that is in better agreement with the 1D kinetics (Figure 4.1b), it allows for leakage of the electronic–electronic signal, and the horizontal projection has quickly decaying tails that lie between the limiting heterogeneous and homogeneous limits (Figure 4.3b).

A.5 Approximating the Microviscosity Distribution

The convolution inherent in kinetic measurements results in a loss of information (equation 51), so the 1D decay spectrum (Figure 4.1b) cannot be uniquely decomposed into its homogeneous and heterogeneous contributions. Fortunately, the loss of information is not complete, and a representative decomposition can be made to illustrate the retained information. The low-order moments of it can be recovered accurately; the loss of information primarily affects higher moments.

The process uses cumulants κ_n, which are combination of moments.[A3] They are additive under convolution. Thus from equation 51,

$$\kappa_n[\hat{C}_{\mathrm{r}}^{(1)}] = \kappa_n[\hat{C}_{\mathrm{hom}}] + \kappa_n[P_{\mathrm{het}}] \tag{A63}$$

holds for the decay spectra. The connection between rate and decay spectra (equation 49) leads to

$$\kappa_n[\hat{C}^{(1)}] = \kappa_n[\tilde{C}^{(1)}] + \kappa_n[\hat{C}_{\mathrm{exp}}^{(1)}]. \tag{A64}$$

Combining these equations gives a relationship between rate spectra,

$$\kappa_n[\tilde{C}_{\mathrm{r}}^{(1)}] = \kappa_n[\tilde{C}_{\mathrm{hom}}] * \kappa_n[P_{\mathrm{het}}]. \tag{A65}$$

The rate spectrum of the 1D rotational decay is easy to find from the form used to represent it, equation A60. We believe that the first four cumulants are meaningful. They are given in Table A.3

To provide a specific model, the homogeneous decay was taken to be a biexponential,

$$C_{\text{hom}}(x) = \tfrac{1}{2}(1+b)e^{-x/x_-} + \tfrac{1}{2}(1-b)e^{-x/x_+}. \qquad \text{(A66)}$$

with a geometric-mean (first moment) of zero. The heterogeneous distribution is assumed to be a smooth, single-peaked function. It should also have sharply defined maximum and minimum values, because the micelle should have well-defined maximum and minimum viscosities. The beta distribution satisfies these criteria and can be easily adjusted to have the desired first four moments.[126] It was used to model the heterogeneous distribution,

$$P_{\text{het}}(\ln T) = \frac{(\ln T - a)^{\alpha-1} + (c - \ln T)^{\beta-1}}{(c-a)^{\alpha+\beta+1} B(\alpha,\beta)}, \qquad \text{(A67)}$$

where $B(\alpha,\beta)$ is the beta function. Equation A67 holds for $a < \ln T < c$; the distribution is zero elsewhere.

The assignment of the cumulants proceeds as follows (see Table A.3). Because the homogeneous decay is defined to have a zero 1st moment, the heterogeneous distribution takes the first moment of the 1D spectrum. The 2D experiment determined that 87% of the 1D 2nd cumulant (d_{rot}) should be assigned to the heterogeneous second cumulant (d_{het}). The 2nd cumulant of the homogeneous decay is then the remaining 13% of d_{rot}. We assumed that the kurtosis of the heterogeneous distribution (ratio of 4th and 2nd cumulants[S3]) was the same as that of the 1D spectrum. The 4th cumulant of the homogeneous decay was calculated by subtraction. The 1st, 2nd and 4th cumulants of the homogeneous decay completely determine the constants in equation A66: $b = -0.742$, $x_+ = 2.12$, $x_- = 0.550$. From these values, the 3rd moment of the homogeneous decay was calculated and subtracted from the 1D 3rd moment to give the heterogeneous 3rd moment.

The first four cumulants of the heterogeneous distribution were then known, so the parameters in equation A67 could be determined:[126] a = ln (1.60 ps), c = ln (1.10 ns), α = 3.25, β = 1.03.

The rotation time of PM597 was measured in a number of solvents, as shown in Figure A.7. All the decays were close to single exponential. The figure reports geometric-mean times versus viscosities. The results were fit to $\bar{T}_r = B\eta$, with B = 31.6 ps/cP. This formula was used to generate the microviscosity scale in Figure 4.4.

Table A.1 Coefficients summarizing the 1D anisotropy and electronic decays[a]

Ti (ps)	2	8	32	128	512	2048	8192	32,768
Anisotropy b	−0.009	0.051	0.029	0.201	0.514	0.214	—	—
Electronic c	0.050	0.007	0.005	0.012	−0.001	0.295	0.824	−0.192

[a] See eq A60. [b] $\tilde{c}^{(1)}_{\mathrm{a},i}$ [c] $\tilde{c}^{(1)}_{\mathrm{e},i}$

Table A.2 Coefficients summarizing the 2D anisotropy–anisotropy (top[a]) and electronic–electronic (bottom[b]) decays.

T_j (ps) \ T_i (ps)	2	8	32	128	512	2048	8192	32,768
2	−0.003 0.003	0.002 0.000	— 0.000	— 0.001	— 0.000	— 0.015	— 0.042	— −0.010
8	0.002 0.000	0.044 0.000	0.031 0.000	— 0.000	— 0.000	— 0.002	— 0.005	— −0.001
32	— 0.000	0.031 0.000	−0.006 0.000	0.036 0.000	— 0.000	— 0.001	— 0.004	— −0.001
128	— 0.001	— 0.000	0.036 0.000	0.119 0.000	0.031 0.000	— 0.004	— 0.010	— −0.002
512	— 0.000	— 0.000	— 0.000	0.031 0.000	0.437 0.000	−0.003 0.000	— −0.001	— 0.000
2048	— 0.015	— 0.002	— 0.001	— 0.004	−0.003 0.000	0.205 0.087	— 0.243	— −0.057
8192	— 0.042	— 0.005	— 0.004	— 0.010	— −0.001	— 0.243	— 0.679	— −0.158
32,768	— −0.010	— −0.001	— −0.001	— −0.002	— 0.000	— −0.057	— −0.158	— 0.037

[a] $\tilde{c}^{(2)}_{\mathrm{aa},ij} = \tilde{c}^{(1)}_{\mathrm{a},i}\tilde{c}^{(1)}_{\mathrm{a},j} + \delta\tilde{c}^{(2)}_{\mathrm{aa},ij}$. See eq A62. [b] $\tilde{c}^{(2)}_{\mathrm{ee},ij} = \tilde{c}^{(1)}_{\mathrm{e},i}\tilde{c}^{(1)}_{\mathrm{e},j}$. See eq A58.

Table A.3 Cumulants calculated on a Ln-T scale

spectrum	κ_1	κ_2	κ_3	κ_4
rotational rate [a]	5.433	1.575	−1.633	7.946
homogenous rate [b]	—	0.205	−0.205	0.247
heterogeneous rate [c]	5.433	1.371	−1.427	6.014

[a] $\tilde{C}_{\mathrm{r}}^{(1)}(\ln T)$ [b] $\tilde{C}_{\mathrm{hom}}^{(1)}(\ln T)$ [c] $P_{\mathrm{het}}(\ln T)$

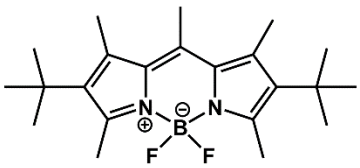

pyrromethene 597

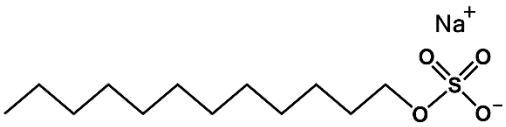

sodium dodecyl sulphate

Figure A.1 Structures of pyrromethene 597 (PM597) and sodium dodecyl sulfate (SDS).

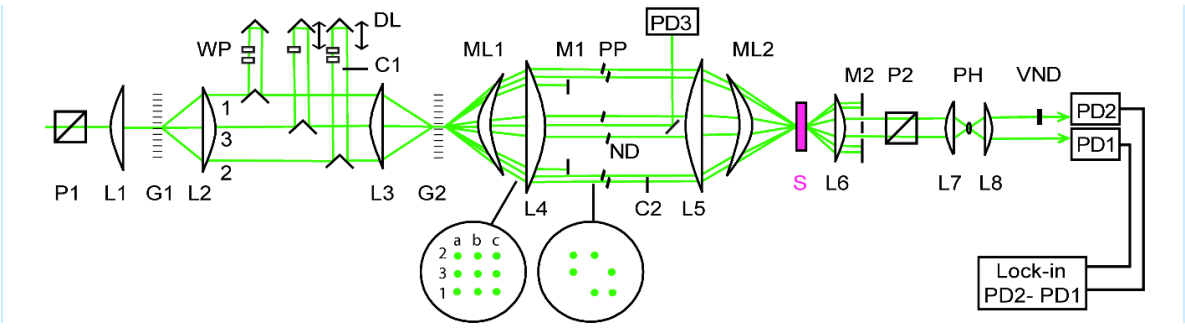

Figure A.2 MUPPETS optical system: polarizers (P), lenses (L), transmission gratings (G), delay lines (DL), meniscus lenses (ML), phase plates (PP), neutral density filter (ND), masks (M), sample (S), pinhole (PH), and photodiodes (PD).

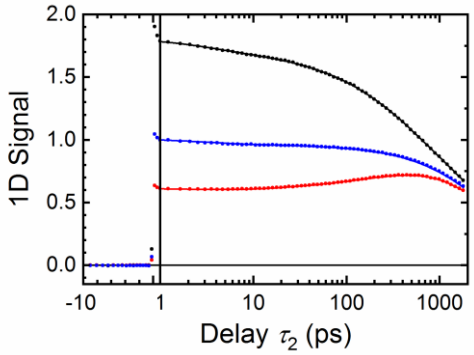

Figure A.3 The raw, 1D pump–probe data for PM597 in SDS micelles: parallel ($\Delta A_{\parallel}(\tau)$, black), perpendicular ($\Delta A_{\perp}(\tau)$ red), and magic-angle ($\Delta A_{m}(\tau)$, blue) polarizations. The scale changes from linear for times <1 ps to logarithmic for times >1 ps. Data are shown as points, and fits to Equation A60 are shown as solid lines.

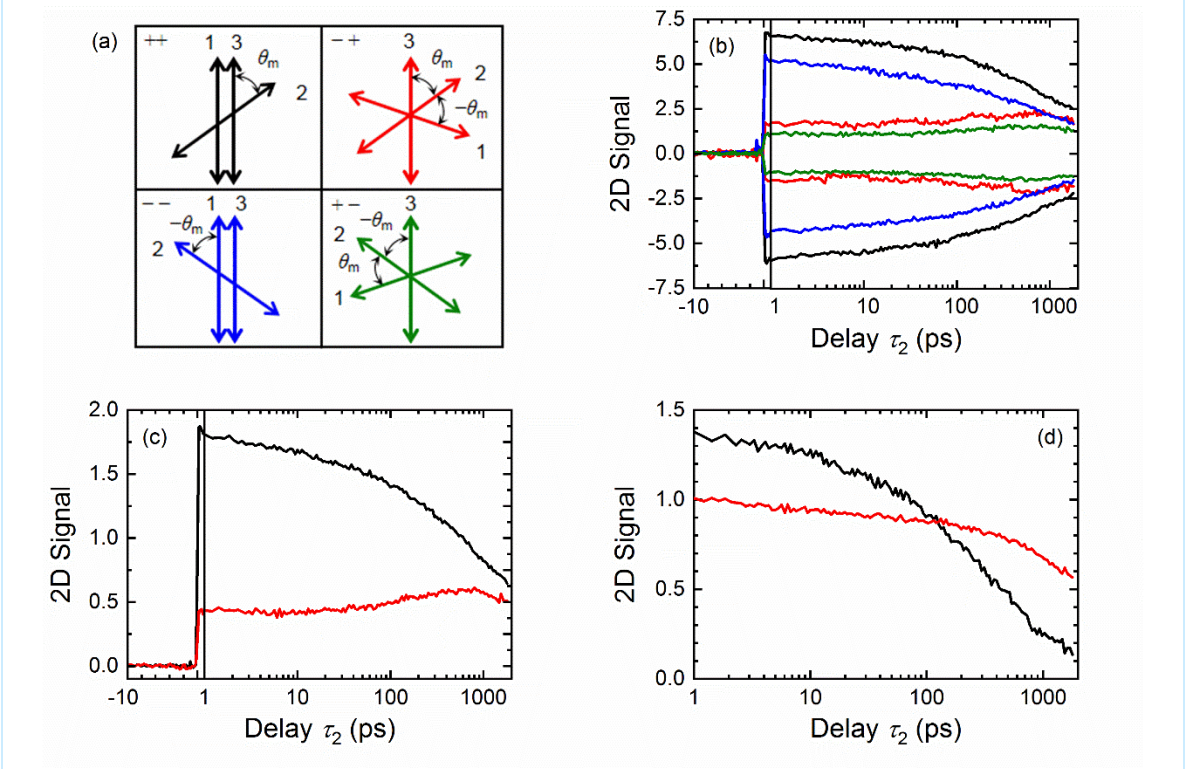

Figure A.4 The MUPPETS data for τ_1 = 1 ps. (a) The polarization of the first (1) and second (2) excitations and of the probe (3) are separated by the magic angle θ_m [measured relative to (2)] to create four polarization combinations. (b) The raw data $\Delta A_p(\tau_2, \tau_1; \varphi)$ with colors corresponding to the polarization conditions in (a). Positive and negative signals correspond to 0° and 180 phases, respectively. (c) The signals $\Delta A_{++}(\tau_2,\tau_1)$ (black) and $\Delta A_{--}(\tau_2, \tau_1)$ (red) are derived by combining the results in (a) (equations A56 and A57). (d) The signals from (c) are added to give the electronic–electronic decay $C_{ee}^{(2)}(\tau_2,\tau_1)$ (Equation 53, red) or subtracted to give the anisotropy–anisotropy decay $C_{aa}^{(2)}(\tau_2,\tau_1)$ (equation A59, black). The time scales in (b) and (c) change from linear for times <1 ps to logarithmic for times >1 ps

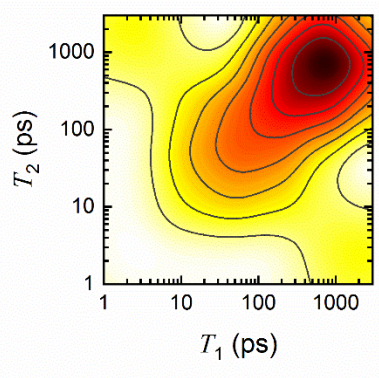

Figure A.5 The 2D anisotropy–anisotropy decay spectrum from the initial fitting to Equation A61 with eight degrees of freedom.

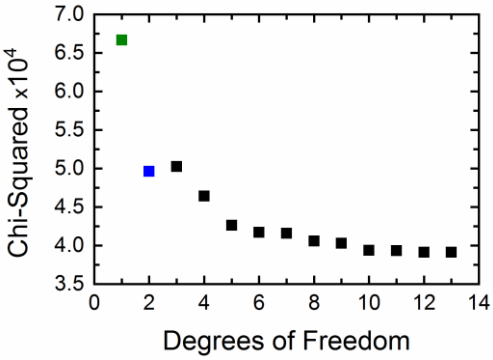

Figure A.6 Chi-squared versus the number of degrees of freedom for the refined fit to the 2D data (equation A62). Green (1 deg. freedom): for the 100% heterogeneous model. Blue (2 deg. freedom): with electronic–electronic leakage added. Black: with homogeneous broadening added.

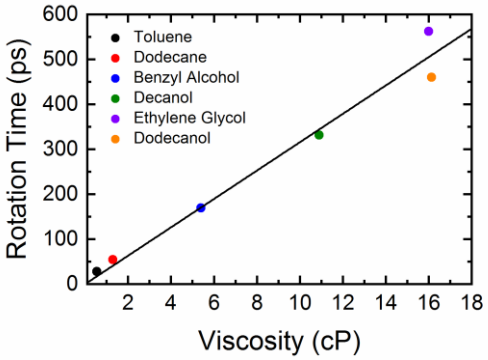

Figure A.7 The geometric-mean rotation time $\bar{T}_r$ of PM597 in various solvents versus their macroscopic viscosities η (points) and a linear fit (line).

APPENDIX REFERENCES

(A1) Khurmi, C.; Berg, M. A. Differential Heterodyne Detection with Diffractive Optics for Multidimensional Transient-Grating Spectroscopy. *J. Opt. Soc. Am. B* **2009**, *26* (12), 2357–2362

(A2) Press, W. H.; Teukolsky, S. A.; Vetterling, W. T.; Flannery, P. P. *Numerical Recipes in C*. Second ed.; Cambridge University Press: Cambridge, 1992.

(A3) Stuart, A.; Ord, J. K. *Kendall's Advanced Theory of Statistics*. Oxford University Press: New York, 1987; Vol. 1.